

SYNTHESIS AND MAGNETO-TRANSPORT MEASUREMENTS IN MAGNETORESISTIVE CORE-SHELL MATERIAL AND 2-D MAGNETIC OXIDES



A thesis submitted towards partial fulfilment of
BS-MS Dual Degree Programme

by

SUVIDYAKUMAR V. HOMKAR

20121077

under the guidance of


DR. ASHNA BAJPAI

RAMANUJAN FELLOW

INDIAN INSTITUTE OF SCIENCE EDUCATION AND RESEARCH PUNE

Certificate

This is to certify that this thesis entitled "Synthesis and Magneto-transport Measurements in Magnetoresistive Core-Shell material and 2-D Magnetic Oxides" submitted towards the partial fulfilment of the BS-MS dual degree programme at the Indian Institute of Science Education and Research Pune represents original research carried out by "Suvidyakumar V. Homkar" at "Indian Institute of Science Education and Research Pune", under the supervision of "Dr. Ashna Bajpai" during the academic year 2016-2017.



Student

SUVIDYAKUMAR V.
HOMKAR



Supervisor

DR. ASHNA BAJPAI

Committee:

DR. ASHNA BAJPAI

DR. SUNIL NAIR

Declaration

I hereby declare that the matter embodied in the report entitled "Synthesis and Magneto-transport Measurements in Magnetoresistive Core-Shell material and 2-D Magnetic Oxides" are the results of the investigations carried out by me at the Department of Physics, Indian Institute of Science Education and Research Pune, under the supervision of Dr. Ashna Bajpai and the same has not been submitted elsewhere for any other degree.



Student

SUVIDYAKUMAR V.

HOMKAR



Supervisor

DR. ASHNA BAJPAI

Acknowledgements

I would like to thank my supervisor, Dr. Ashna Bajpai for all the guidance, advice and encouragement provided by her during my time as her student. I feel lucky to have worked with a supervisor who cared so much about my work, and who always helped me understand complexities involved in experimental work and the way to tackle them. I am really grateful for the opportunity given by her to work in the lab.

I would like to thank my lab members, Namrata for helping me in hydrothermal synthesis work and for her willingness to help in even tiniest of issues, Aakanksha for her constant support to my work and interesting discussions related to philosophy and politics, Nitesh for his fruitful discussions on basic aspects of science and for taking my mind away from research at times.

I take this opportunity to thank Dr Surjeet Singh and his lab members Prachi Telang, Rabindranath Bag for helping me in magnetoresistance measurements.

I would like to thank Dr. Sunil Nair for his continued support of my work and valuable suggestions in synthesis and characterization of SrRu_2O_6 . I would like to thank him and his lab members Charu Garg and Soumendranath Panja for helping me in Magnetic measurements.

I would like to thank the technical staff in h cross, Nilesh Dumbre, Anil Shetty, T.S.Yatish and Prashant Kale for their support.

I would like to thank all my friends for the wonderful time we had at IISER and also for being there with me through tough times.

I would like to thank IISER for giving me this platform to do research and DST for INSPIRE fellowship.

Finally, I would like to thank my parents and grandparents who continually supported and motivated me to continue my work and who helped me morally to get through all the ups and downs of research. I would like to thank my brother for his constant entertainment at home.

Abstract

This thesis is in two parts: First part relates to tuning of the granular magneto-resistance (MR), which naturally occurs in systems consisting of ferromagnetic (FM) metallic grain and antiferromagnetic (AFM)/ insulating grain boundary(GB). We have explored Ni-NiO system with varying grain size and morphology. Magneto-resistance (MR) measurements on various samples have been made using standard four probe resistivity technique. Low field MR data shows an anomaly at 250 K in Ni-NiO sample with crystalline hexagonal Ni plates. This is likely to be due to the variations in the grain size as well as the magnetic interactions between the FM grain and the AFM GB.

In second part of thesis, synthesis, characterization and magnetization measurements on a relatively unexplored layered 4d magnetic oxide, SrRu_2O_6 are presented. Graphene like 2-D sheets of this oxide have been obtained using the technique of "Liquid Exfoliation" for the first time. Same technique has also been employed to obtain 2-D sheets of Na_2IrO_3 as well. Preliminary measurements reveal micron sized sheets in case of SrRu_2O_6 , and nano scale rectangular sheets in case of Na_2IrO_3 with significant yield. Exfoliation process in these two samples has been checked for reproducibility and yield factor for multiple times. Further experiments are required to obtain the layer thickness and composition in each case. Thermo-remnant magnetization (TRM) data on the bulk samples show finite remanence which hints toward the possibility of magneto-strictive effects in both the systems.

Contents

1	Introduction	4
1.1	Magnetism	4
1.1.1	Paramagnetism	5
1.1.2	Ferromagnetism	5
1.1.3	Antiferromagnetism	6
1.1.4	Transition Metal Oxides (TMO)	8
1.1.5	Frustrated systems	9
1.2	Magnetoresistance and Magnetostriction	10
1.2.1	Magnetic Tunnel Junction	10
1.2.2	Magnetostriction	10
1.2.3	Ni-NiO core shell	12
1.3	Layered materials	12
1.3.1	Layered TMO : Graphene like 2-D Magnetic Oxides	13
1.3.2	SrRu ₂ O ₆	14
1.3.3	Na ₂ IrO ₃	14
1.4	Plan of thesis	17
2	Methods	18
2.1	Sample Preparation	18
2.2	Liquid Exfoliation Technique	18
2.3	Powder X-ray Diffraction	19
2.4	Scanning Electron Microscope (SEM)	20
2.5	Raman spectroscopy	21
2.6	Magnetic Measurements using MPMS	22
2.7	Magnetoresistance measurement in PPMS	23

2.8	Probe station	24
3	Synthesis, Characterization and magnetic measurements of bulk and 2D SrRu₂O₆	26
3.1	Sample Preparation and Characterization	26
3.2	Magnetic measurements	28
3.3	Liquid exfoliation	30
3.3.1	Bulk exfoliation	32
3.3.2	Raman spectroscopy	33
4	Magnetic measurements and Exfoliation of Na₂IrO₃	34
4.1	Sample Characterization	34
4.1.1	Raman Spectroscopy	34
4.1.2	I-V characterization	34
4.2	Magnetic measurements	36
4.3	Liquid exfoliation	38
5	Magnetoresistance measurements in Ni-NiO system	40
5.1	Sample Characterization	40
5.1.1	Hexagonal plates (HP)	41
5.1.2	Rod-like particles	42
5.1.3	Spherical particles	42
5.1.4	Thin Sheets	42
5.1.5	Raman Spectroscopy	44
5.2	Resistivity measurement	45
5.2.1	Effect of magnetic field	45
5.2.2	Effect of heating	47
6	Summary and Future work	49
6.1	Summary	49
6.2	Future Plans	50
	References	51

Chapter 1

Introduction

1.1 Magnetism

The history of magnetism dates back to ancient era when lodestones were used to attract iron pieces [1]. After discovery of lodestones (greek term means stone from magnesia), many applications of this new discovery started to emerge. In middle ages, chinese and european scientists were the first ones who used the concept of magnetism in building compass for navigational purposes [2]. First modern day literature on experiments in magnets and evidence of earth having its own magnetic field is given by William Gilbert in his book *De Magnete* in 16th century. The relation between electricity and magnetism was not known until 19th century when, this relationship was established through experiments by Hans Oersted and Ampère. Further experiments by Carl Gauss, Jean-Baptiste Biot and Félix Savart found several connections between electricity and magnetism. James maxwell unified these separate concepts through Maxwell equations and gave rise to new field of electromagnetism [1]. This field continued to develop in 20th and 21st century especially due to advancements in quantum mechanics.

Magnetic materials are primarily categorized into ferromagnetic, antiferromagnetic, paramagnetic and diamagnetic. In the present work, we have explored various magnetic material including 3d, 4d and 5d transition metal and their oxides. Some relevant technical terms are briefly explained in the following.

1.1.1 Paramagnetism

Paramagnetic materials have permanent magnetic dipole moments i.e., spins due to unpaired electrons in its valence shell. In absence of magnetic field, no particular order exists in paramagnetic materials due to random thermal fluctuation in the material causing all spins to point in random directions giving zero net magnetization. In the presence of magnetic field all the spins align in its direction because of torque applied on all the spin through this external field. If the field is switched off, the paramagnetic materials relax to its random spin orientation configuration and does not retain any remanence. Magnetic susceptibility of paramagnet increases with decrease in temperature and follows Curie-Weiss law [3].

$$\chi = \frac{C}{T - \theta} \quad (1.1)$$

where C = Curie-weiss constant, χ = Susceptibility, T= Temperature, θ = Transition temperature.

The graph in figure 1.3 (b) shows paramagnetic behaviour in susceptibility versus temperature graph. The plot of $\frac{1}{\chi}$ vs T gives a linear graph and the values of slope and intercept gives information about C and θ . For ideal paramagnet, θ in equation 1.1 is zero. For materials with paramagnetic behaviour at high temperature and ferromagnetic or anti-ferromagnetic behaviour at lower temperatures, θ signifies the transition temperature.

Paramagnetic, Ferromagnetic and Antiferromagnetic materials have at least one unpaired electron but in diamagnetic material there are no unpaired electrons and hence in the presence of magnetic field give negative susceptibility as the motion of electron around their atom opposes the external field due to Lenz's law.

1.1.2 Ferromagnetism

Ferromagnetism in materials arises due to the tendency of electrons' intrinsic angular moment i.e., electrons' spin to align in parallel configuration with neighbouring electrons' spin. This holds true for substances with unpaired electrons in their system. Even in the absence of magnetic field, ferromagnet have spins parallel to each other, but as the number of spins parallel to each other increases, the substance becomes unstable and to

achieve a lowered energy state, magnetic domains are formed. These domains act like a tiny permanent magnet and in the absence of magnetic field, the orientation of domains is such as to negate magnetic field produced by them. Application of magnetic field causes the domains to start aligning in the direction of magnetic field and after certain critical magnetic field, all domains gets aligned and magnetization saturates. Interestingly, removal of the magnetic field does not demagnetize it completely and some remanence stays in the substance. Figure 1.1 shows a typical M-H hysteresis curve of ferromagnets. All ferromagnets have a critical temperature called 'Curie temperature' above which they are paramagnetic [4]. This is due to destruction of parallel ordered state by random thermal fluctuations. Figure 1.3 (a) shows characteristic M-T curve for ferromagnet. The Heisenberg exchange energy of two interacting spins is given by equation 1.2. The material is ferromagnetic only if the exchange coupling constant J between two interacting spins is positive. Exchange coupling is of two main types; direct exchange and indirect exchange. Indirect exchange interaction is further divided into double exchange, superexchange and RKKY interactions [fig 1.2]. Ferromagnetism in materials is a consequence of either direct exchange or double exchange interaction. In direct exchange, electrons on two different magnetic atoms can interact directly due to close proximity between the atoms whereas in double exchange, electrons on two magnetic atom interact through another non-magnetic atom between them. Double exchange occurs only when one atom has an extra electron than the other atom. Most commonly, ferromagnetism is seen in transition metal element Iron, Cobalt and Nickel.

$$H = -2JS_1.S_2 \quad (1.2)$$

1.1.3 Antiferromagnetism

Antiferromagnetism occurs due to electron spins on neighbouring atoms aligned anti-parallel to each other. Simple antiferromagnets have local moments on two inter-penetrating sublattices of same structure [3]. In absence of external magnetic field the net magnetization of antiferromagnets is zero because of anti-parallel alignment of magnetic moments which neutralize each others magnetic field. In presence of external magnetic field the magnetization in one of the sub-lattice external magnetic field is more than other sublattice and hence a net magnetization is obtained. The temperature below which

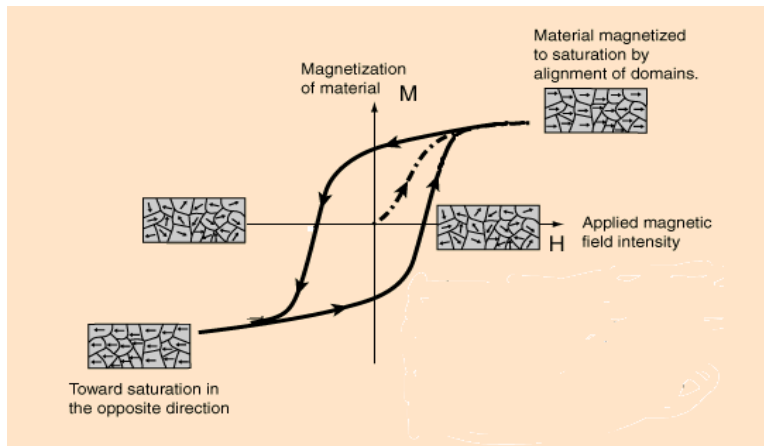


Figure 1.1: Typical M - H curve for ferromagnet showing state of magnetic domains at each stage.[5]

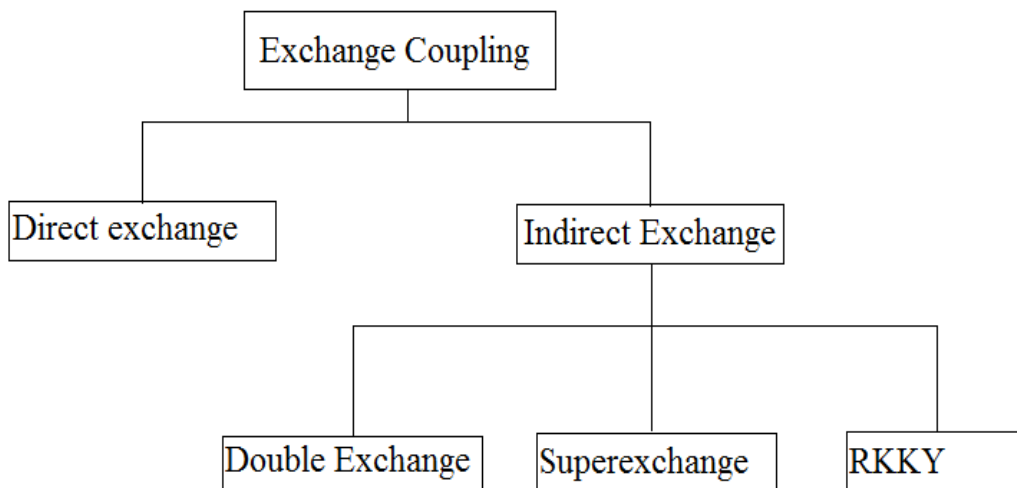


Figure 1.2: Various types of exchange interactions.

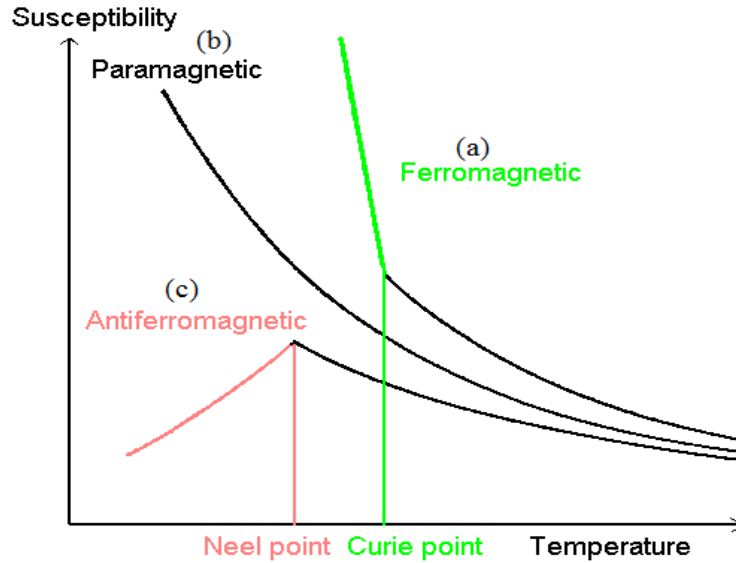


Figure 1.3: *Susceptibility vs Temperature curve for (a) Ferromagnet, (b) Paramagnet, (c) Antiferromagnet. [6]*

antiferromagnetism can be observed is termed as Néel temperature after Louis Néel who discovered it. As can be seen in figure 1.3 (c), susceptibility is highest at Néel temperature and reduces below this temperature. This is due to reduction in thermal energy at low temperatures which helps magnetic energy to dominate [4]. The material is antiferromagnetic only if exchange energy coupling constant J in antiferromagnetic compound is negative. Most commonly antiferromagnetism is observed in oxides due to superexchange interaction between them. In this type of interaction, magnetic atoms with same valence electrons interact through a non-magnetic atom.

1.1.4 Transition Metal Oxides (TMO)

Transition metal oxides are known to exhibit exotic properties such as metal insulator transition, superconductivity, multiferroicity etc, due to the presence of electronic correlations. These properties are the consequence of interplay between the on site Coulomb interaction U and the bandwidth W . In 3d magnetic oxides, such as NiO, the band theory predicts metallicity but due to the magnitude of U , the system can be insulating. In TMOs with high atomic number such as 4d and 5d system, the spin orbit coupling also plays an important part and comparable energy scales of U , W and Spin Orbit coupling gives rise to even more exotic states of matter such as QSL, Topological Insulators etc

[7]. Spin orbit coupling in materials with high atomic numbers goes as Z^4 where Z is the atomic number [7] and hence it is found to be more in the case of TMO with 4d and 5d transition metal.

A new class of 4d and 5d TMO's with high transition temperature has emerged recently. Compounds of this class have transition temperature well above room temperature and by suitable doping the transition temperature could be brought down to room temperature which would then be possible to incorporate into room temperature devices. Some of the discovered compounds of this class are CaTcO_3 , SrTcO_3 and NaOsO_3 systems but due to radioactive element Tc and toxic element Os, these materials cannot be directly applied in scalable application [8]. Hence compounds in this class with large scale compatibility are being explored.

1.1.5 Frustrated systems

Frustrated systems in context of magnetism exist when a particular system has arrangement of spins such that there are more than one ground states. One of the example given for a system of geometrical frustration is illustrated in figure 1.4 where neighbouring spins tend to have antiferromagnetic configuration and in this triangle there exist 2 equally probable possibilities for spin direction in third position. Similar type of geometrical frustration in 3D analogue is seen in tetrahedron. Systems which exhibit geometrical frustration are Kagome lattice, honeycomb lattice, certain pyrochlores, systems with spinel structure [9]. There is possibility for realization of exotic physics with emergent properties in such systems.

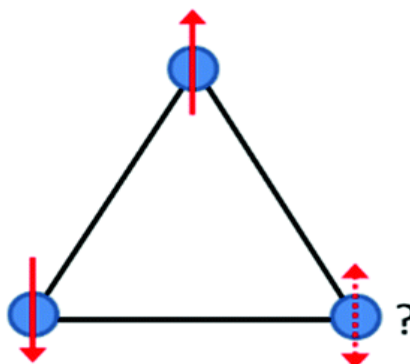


Figure 1.4: Geometrical frustration in a 2D triangle can be observed [10]

1.2 Magnetoresistance and Magnetostriction

1.2.1 Magnetic Tunnel Junction

Magnetoresistance (MR) is the change of resistance in a particular material due to application of magnetic field. Conventionally, resistivity measurements are made at different magnetic fields and equation 1.3 is used to calculate % MR. First application of this effect was in anisotropic magnetoresistance (AMR) devices used as read head sensors in hard disk drives. With time, disk storage density increased and consequently the need for read head sensors with high MR also increased. This paved the way for discovery of Giant Magnetoresistance (GMR) and Magnetic tunnel junction (MTJ) devices [11].

$$\%MR = \frac{\rho(H) - \rho(0)}{\rho(0)} \quad (1.3)$$

MTJ has two ferromagnetic conductors separated by thin dielectric layer called barrier layer. Electrons can tunnel through this thin layer resulting in conduction. Figure 1.5 shows the tunnelling phenomenon due to wave nature of electron where evanescent wave of electron can be seen in the barrier. The tunnelling mechanism gives a finite resistance which can be tuned in an MTJ by altering the magnetization direction of ferromagnetic conductors by applying magnetic fields. This effect is called tunnelling magnetoresistance (TMR) and it has been observed that this resistance is low if the ferromagnetic conductors have parallel magnetization and high if they are anti-parallel. Fundamental reason for TMR phenomenon is the variation in electronic density of state (DOS) at fermi level between spin up and spin down electrons. As the spin is conserved while tunnelling, electrons only tunnel into spin band of same orientation and as the configuration is changed we get exchange between two spin subbands of one electrode as can be seen in fig 1.6 [11].

1.2.2 Magnetostriction

Magnetostriction is property of certain magnetic materials to change their dimensions and shape due to application of magnetic field [12]. The reason for change in dimensions is related to the rearrangement of structure in the compound so as to align the easy axis of magnetization in sample with the external magnetic field to achieve lower energy

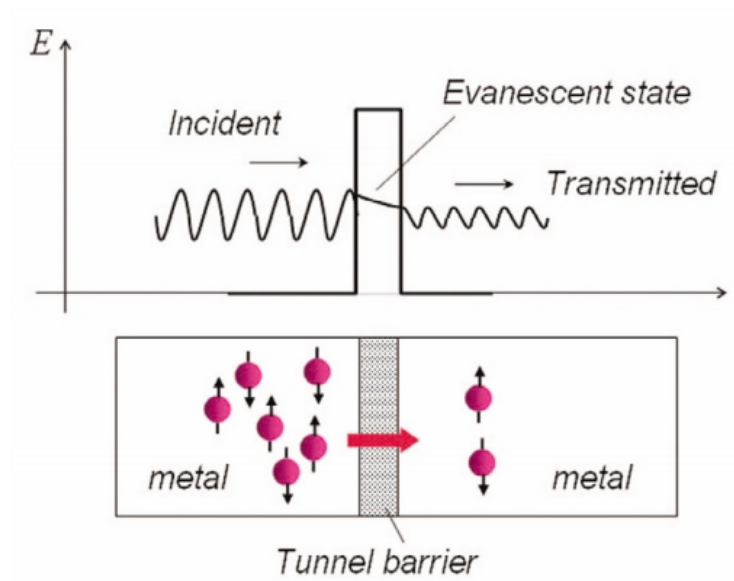


Figure 1.5: Figure shows schematic of tunnel barrier phenomenon. [11]

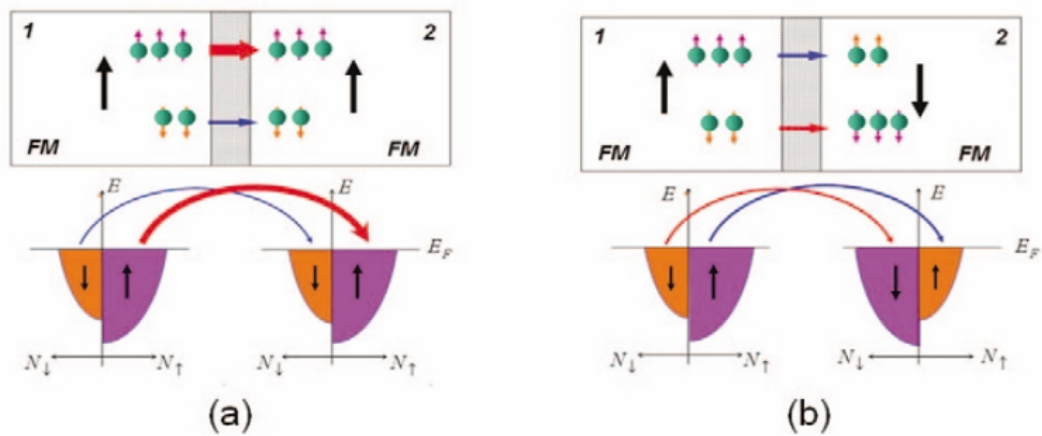


Figure 1.6: (a) Tunnelling for FM conductors in parallel alignment and their spin bands configuration (b) Tunnelling for FM conductors in anti-parallel alignment and their spin bands which shows switching of one band [11]

state [13]. Easy axis in magnetic materials is the axis at which the magnetic dipoles are easily aligned as compared to other direction and is a consequence of existing magneto-crystalline anisotropy in the materials. This magneto-crystalline anisotropy arises due to spin-orbit coupling in the materials [14]. As mentioned in TMO subsection, spin orbit-coupling is found to be higher in TMO's and therefore there is a possibility of high magnetostriction effect in these compounds. In present work, magnetostriction effect is probed in 4d SrRu_2O_6 and 5d Na_2IrO_3 TMO.

1.2.3 Ni-NiO core shell

In Nickel-Nickel Oxide core shell structure, nickel (Ni) is the core and nickel oxide (NiO) is the shell. This system has Ni which is ferromagnetic conductor and NiO which is an antiferromagnetic insulator and hence Ni-NiO-Ni can form a MTJ type of system with thin layer of NiO and high tunneling magnetoresistance can be expected due to $\sim 30\text{-}40\%$ spin polarization in Ni [15]. It has been shown that in such systems, enhanced magnetoresistance can be obtained with increasing grain size and change in morphology due to a different type of tunnelling mechanism called fluctuation induced tunnelling (FIT) [16]. FIT occurs when a material in a heat bath has thermal fluctuations on both sides of grain boundary and hence gives rise to extra voltage in addition to applied one. Various other effects due to influence of thin layer in such systems has been discussed in [17]. Bajpai et.al., in [16] argue that the effect of coulomb blockade (CB) which dominates in nano-metre size grains is suppressed in micro-metre size grains of half metallic $\text{CrO}_2\text{-Cr}_2\text{O}_3$ system with core-shell structure and similar FM/Conductor-AFM/Insulator boundary as in Ni-NiO system.

1.3 Layered materials

Graphene was the first 2D material to be mechanically exfoliated from graphite and had significant change in properties from graphite like high mechanical strength, increased conductivity, quantum spin Hall effect etc., [18] which triggered interest in the field of 2D materials. This change in characteristic properties could have many reasons like, increase in total surface area, change of 3D wave-function into 2D one and restricted interactions of electrons into 2. Although graphene had such exotic properties it could not directly

be incorporated into electronic devices which require semiconductors and resistors too for its functioning [19]. In search for 2D material with band gap for electronic industry applications, researchers discovered many 2D materials like MoS₂, WS₂ etc which were later converted into devices like Field Effect Transistor (FET) and photoemission detectors [20, 21, 22, 23]. Due to radically different effects demonstrated by 2D materials compared to 3D counterparts, synthesis and optimization of these 2D materials became a very important issue and new techniques to obtain these materials emerged of which exfoliation of layered materials seemed a promising and important tool. Exfoliation techniques can yield nanometre or even atomically thin sheets which is then categorized as 2D material.

Materials which have strong intra-plane bonding in two dimension but very weak inter-plane bonding in third dimension are called layered materials [18]. These materials can be visualised as many 2D layers stacked over each other to form the 3D structure. These layers can be separated from each other by shearing the weak bonds between them and the process of separation is termed as exfoliation. Primary methods of exfoliation are mechanical exfoliation, chemical exfoliation and solvent assisted exfoliation (liquid exfoliation) [24]. In liquid exfoliation technique, material is dispersed in a solvent and ultrasonicated to separate the layers. This technique gives high yield and is industrially scalable. Chemical exfoliation technique uses intercalating agent like lithium to penetrate between layer gaps to separate them followed by sonication to disperse them. Mechanical exfoliation is made by separating sheets through adhesive tape [25]. Apart from exfoliation techniques there also exist other chemical routes to obtain 2-D sheets like Chemical Vapour Deposition and colloidal synthesis [19].

1.3.1 Layered TMO : Graphene like 2-D Magnetic Oxides

2-D materials such as graphene and MoS₂ have been explored extensively in the recent past. However 2-D magnetic oxides are hardly explored. Since TMO exhibit plethora of interesting and emergent properties in three dimension, the ability to obtain 2-D sheets of TMO may give rise to not only tailor and tune these properties but also new properties can emerge [26]. Some of the recently discovered layered TMO's are 4d SrRu₂O₆ and 5d Na₂IrO₃ which shows emergent properties in bulk form. Due to inherent layered

structure there is possibility for separation of graphene like 2D layers in this compound. An attempt has been made in present work to show the preliminary results indicating 2D sheets formation in these compounds. The 4d and 5d based TMO discussed here have not been exfoliated using liquid exfoliation to the best of our knowledge.

1.3.2 SrRu₂O₆

SrRu₂O₆ is a transition metal oxide (TMO) which adopts hexagonal $P\bar{3}1m$ structure and has alternating layers of Sr and edge shared RuO₆ octahedra [fig 1.7]. It is a G-type antiferromagnetic compound with Néel temperature of 565 K [fig 1.8] which is highest among 4d TMO's [27]. It can be seen in figure 1.8 (b), there is linear increase in susceptibility above 565K temperature which pertains till 750K. It is suspected that this could be due to existence of 2D magnetic correlations above transition temperature [28]. This material has strong in-plane magnetic interaction because of antiferromagnetic superexchange coupling between Ru atoms mediated by O and weak inter-plane magnetic interactions which are necessary for long range 3D order [28]. High transition temperature in pure 4d and 5d transition metal oxides has been found in other compounds like SrTcO₃, CaTcO₃ and NaOsO₃ but SrRu₂O₆ is first to have high transition temperature and quasi-2D structure which therefore provides a playground for exotic physics in this compound [8]. High ordering temperature phenomenon in SrRu₂O₆ is attributed to high degree of co-valency between Ru and O atoms [8]. Hiley et al. in ref [27] have reported lattice parameter change in SrRu₂O₆ which could be a hint for magneto-strictive effects in this compound.

1.3.3 Na₂IrO₃

Na₂IrO₃ is a 5d transition metal oxide with layered structure. The material adopts monoclinic C2/c structure with alternating stacked layers of Na and edge shared NaIr₂O₆ [fig 1.9]. This compound is antiferromagnetic with zig-zag ordering below 15 K [see fig 1.10] but weak magnetic correlations exist even at higher temperatures [30]. This is related to geometrical frustration or 2D magnetic interactions in this compound. It can be seen from figure 1.9 that this material has honeycomb lattice structure. The possibility of magnetic frustration and existence of honeycomb lattice structure in this compound makes it strong candidate for quantum spin liquid (QSL) in Kitaev model [31]. QSL

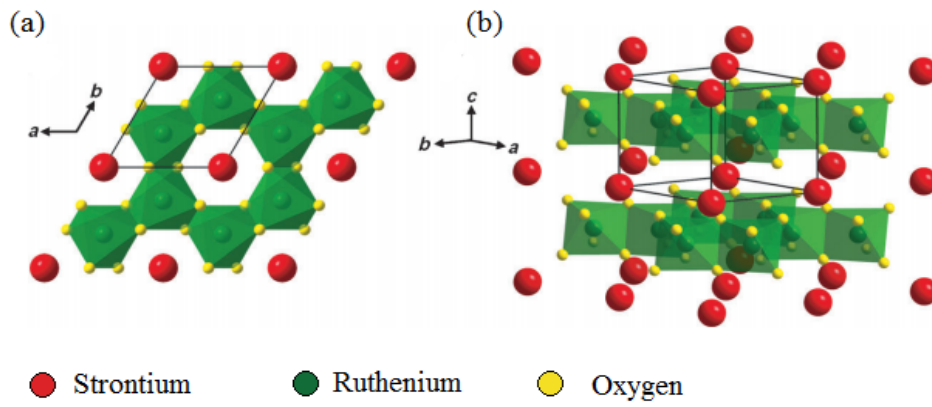


Figure 1.7: (a) Geometric structure as seen from *ab* plane (b) Separate layers of Sr and RuO₆ octahedra and their combination in *abc* plane [29]

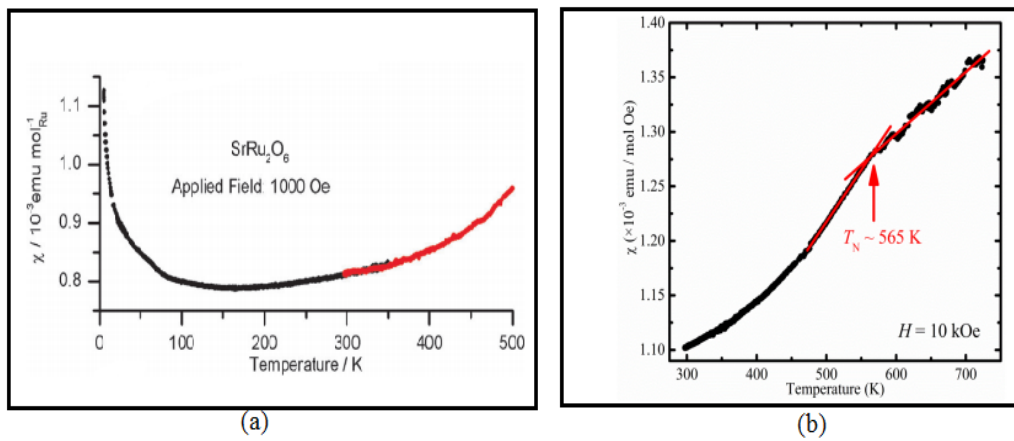


Figure 1.8: Susceptibility versus temperature plot (a) from 2K to 500K (b) from 300K to 750K [29, 27]

system occurs due to existence of many degenerate ground state leading to magnetic frustration. Because of frustration, the system behaves like in a magnetically liquid state.

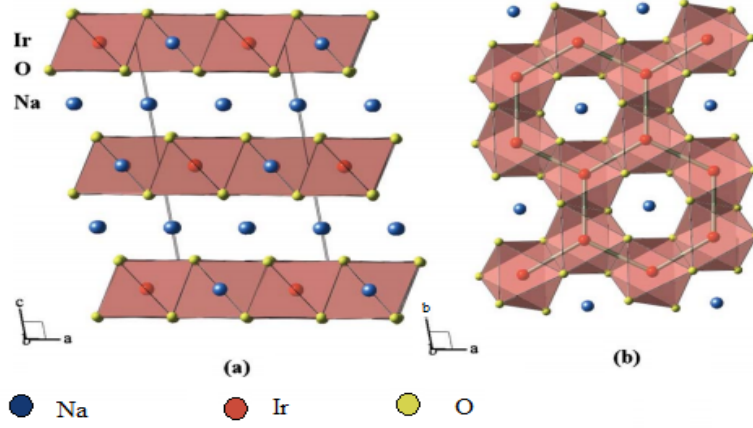


Figure 1.9: (a) Separate layers of Na and NaIr_2O_6 octahedra seen in c-a plane (b) Honeycomb lattice structure as viewed in a-b plane [30]

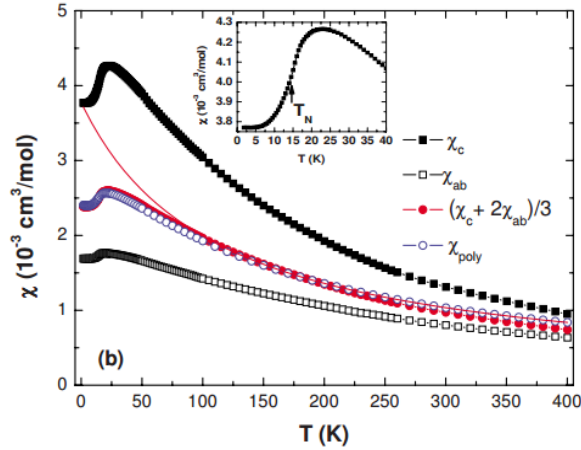


Figure 1.10: Figure shows temperature dependence of susceptibility in polycrystalline powder and single crystals with magnetic field parallel to c axis and ab plane. [30]

Consequently, long range ordering is not seen till very low temperatures and magnetic correlation also exist above transition temperature. Possibility of QSL in this system is further supported by the evidence of broad band in Raman spectra at lower temperatures in Na_2IrO_3 [32] which is correlated with existence of liquid like state. One of the evidence which opposes Kitaev model possibility is the report of Ir-O-Ir bond angle deviation from 90° which is essential for Kitaev interactions [33]. It can be seen from inset of figure 1.10

that maximum in susceptibility occurs above the actual transition temperature. Yogesh Singh et.al., in [30] suggest that this could be due to development of short range order above T_n in layers of NaIr_2O_6 which indicates that Na_2IrO_3 is a quasi 2-D material.

1.4 Plan of thesis

Due to high spin orbit coupling and apparent 2D structure in layered 4d and 5d transition metal oxides, a plethora of interesting properties remain to be investigated. In first part of this thesis, we aim to synthesize and characterize SrRu_2O_6 compound followed by magnetic measurements in SrRu_2O_6 and Na_2IrO_3 . Liquid exfoliation of SrRu_2O_6 and Na_2IrO_3 into their 2D counterparts is also envisaged.

There has been high demand of MTJ systems with high magnetoresistance (MR) for varying applications. To meet this demand, variety of systems with possibility of high MR are tuned and studied. In second part of this thesis, we aim to synthesize and tune parameters like shape and morphology in Ni-NiO system and optimize MR by doing resistance measurements at different magnetic fields.

Chapter 2

Methods

2.1 Sample Preparation

Samples used in this work have been synthesised following hydrothermal route, wet chemical route for the synthesis of nano and mesoscopic metal and metal oxide particles. The 2-D sheets of the metal oxides have been obtained using a relatively new technique called Liquid Exfoliation of layered materials . While the first two synthesis procedure are well established, the liquid exfoliation technique , which can be used to significantly enhance the yield of 2-D material, is described in greater detail in the following section.

2.2 Liquid Exfoliation Technique

2-D material are important for both fundamental and technological reasons. Here two issues are important. First is to obtain large size of the mono-layer material and second is the scalability factor. For instance, Mechanical exfoliation is known for obtaining monolayers of graphite, the graphene. However, this technique may not be practical for device application where large number of such sheets are required.

Among all the techniques employed for obtaining large quantity monolayers of any 2-D material, liquid exfoliation is relatively simple method, consisting of a few sessions of sonication and centrifugation [18]. The mechanical vibrations due to sonication enable isolation of weakly coupled layers and a suitable choice of the solvent maintains the layers separated and dispersed in the solvent. This is depicted in figure 2.1 taken from [18]. Depending on the material, this technique requires optimization of experimental

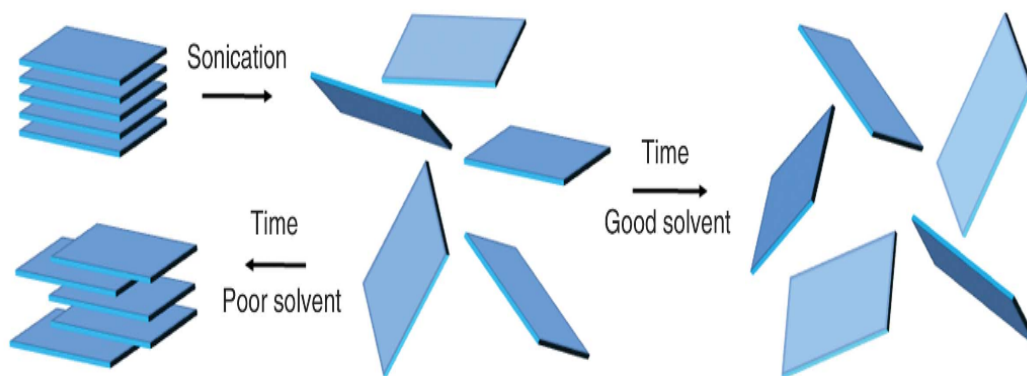


Figure 2.1: *Figure shows coagulation of separated sheets due to poor solvent and maintained dispersion of sheets due to good solvent with time. [18]*

conditions to find the suitable solvent and optimize the sonication and centrifugation time.

In present work, techniques of bath sonication and probe sonication were used. In bath sonication, the sample suspended in solvent is exposed to ultrasound from outside the glass beaker, whereas, in probe sonication the probe is immersed in solvent and exposed to ultrasound directly. Probe sonicator used here is from Oscar ultrasonics of model SonaPros PR-250MP. Parameters like intensity of ultrasound, sonication time and time gap between successive events can be modulated in this instrument. Centrifugation was carried out in Micro-200R 2405 obtained from Hettich zentrifugation.

2.3 Powder X-ray Diffraction

Powder X ray diffraction provides structural information of the material and is useful for identification of phase, degree of crystallinity and the lattice parameters of the sample. In this type of diffraction method, all planes are equally exposed statistically as compared to a single crystal where one plane is predominant. All compounds have a characteristic diffraction data with peak positions at specific 2θ value for different planes which acts as a ‘fingerprint’ for each compound. The peak positions are determined by the distance between parallel planes and is given by Bragg’ s law,

$$2d\sin(\theta) = n\lambda \quad (2.1)$$

where d=Distance between planes, θ = Incidence angle, λ = Light wavelength.

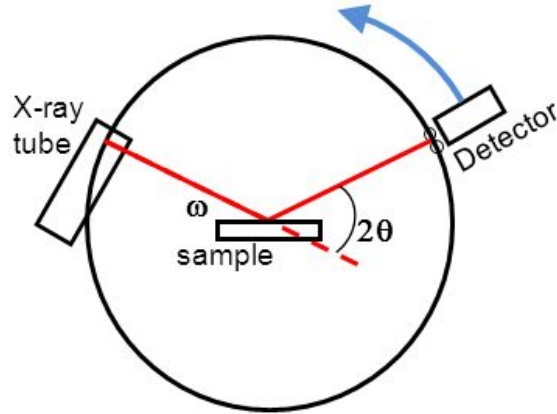


Figure 2.2: An illustration of P-XRD set up. [34]

In an x-ray diffractometer [fig 2.2], x-ray tube and detector move on the periphery of a circle and sample at its center. If X-rays are focused on the sample at an angle of θ which satisfies bragg's law then the beam gets diffracted at 2θ angle from the original beam. Powder samples were characterized by X-ray diffraction using Bruker D-8 advance with copper $K\alpha$ ($\lambda=1.54$) radiation source. Intensity versus 2θ diffraction data was obtained from 2θ range of 10° - 90° and step size of 0.0196° .

2.4 Scanning Electron Microscope (SEM)

A scanning electron microscope is employed to obtain information about the morphology, size and chemical composition (EDX) of polycrystalline samples. SEM is particularly useful over conventional optical microscopes as it can resolve images till 20 nm and hence is a very important tool in imaging nano-materials.

In SEM imaging, an electron beam is used instead of light beam and is focused onto the sample using electromagnetic lens. The sample is scanned using horizontal and vertical movements of specimen stage. The interaction of electron beam with the sample at various depths produces different signals. The signals generated at increasing depths are from Auger electrons, secondary electrons, back-scattered electrons, characteristic x-rays of elements respectively as shown in fig 2.3. Secondary electrons are generated due to emission of valence electron from the surface atoms and are used to obtain topographical information and used for image formation. Back-scattered electrons are just the reflected electrons from within the sample and can also be used to determine information about

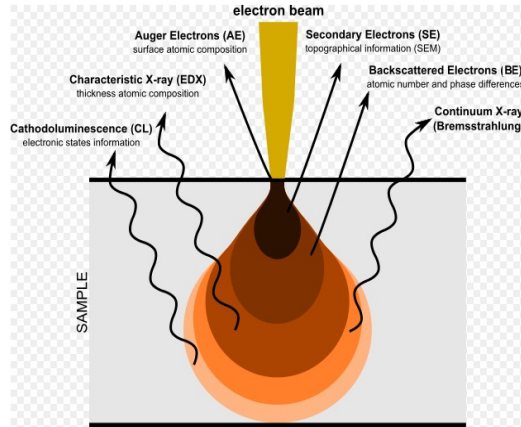


Figure 2.3: Illustration of different signals generated at different depths after electron beam hits sample. [35]

the atomic number. Characteristic x-rays are emitted by elements bombarded by high energy electrons and are used to understand the elemental composition of the material using technique of energy dispersive analysis of x-rays (EDAX).

SEM instrument used in this project is provided by Zeiss Ultra Plus. All images are taken by detecting secondary electrons and in either SE2 or In-lens mode. SE2 detection mode is for low energy secondary electrons for imaging surface with high contrast and In-lens for high energy secondary electrons for imaging electronic variations/differences in work function with high resolution.

2.5 Raman spectroscopy

Raman spectroscopy is used as a characterization tool in solid state physics as it can probe certain vibration modes from quasiparticles like phonons, plasmons and magnons which are characteristic to certain type of solid state material. In Raman spectroscopy, a beam of monochromatic light from laser, typically in the wavelength range of visible and ultraviolet is used to probe the sample. The sample emits some radiation back after interacting with laser light and this light is collected in the detector. The photon from the laser light can interact elastically or in-elastically with the particles. Elastic interaction excites the particle in a higher vibrational state and the particle scatters back the photon of same wavelength to reach the ground state and this type of scattering is called ‘Rayleigh scattering’. Particles which interact in-elastically with the photons reach

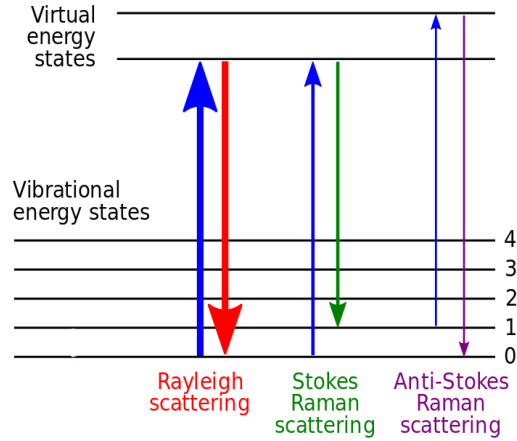


Figure 2.4: *Energy level diagram of Raman scattering effect. [36]*

a short lived virtual state and emit either higher or lower energy light compared to the incident light. Lower energy light is emitted if a particle in ground state is excited to virtual state and relaxes back to a higher vibrational state instead of ground state and higher energy is emitted if particle from higher vibrational energy relaxes back to ground state from the virtual state [fig 2.4]. Lower light energy can be seen as left shifted from Rayleigh line on wavenumber co-ordinate and is called ‘Stokes shift’, whereas higher light energy is seen to be right shifted on wavenumber co-ordinate and is called ‘Anti-Stokes shift’.

Raman spectroscopy instrument from Horiba company was used to characterize the samples and to identify different raman modes. Laser light of 488nm (blue light) was used for excitation and video mode with 20x and 50x lens was used to image the sample and select area of choice. Confocal microscope for imaging is obtained from Olympus instruments.

2.6 Magnetic Measurements using MPMS

Magnetic property measurement system (MPMS) is a magnetometer built by quantum design and is used for high sensitive magnetization measurements. In MPMS instrument, a small amount of sample (about 20-50 mg) is kept packed in a non-magnetic capsule which is further kept at the centre of a non-magnetic straw. This sample is loaded into a liquid helium chamber and is positioned at the centre of pick up coils which in turn is located at centre of the superconducting magnets. A current is generated in pick up coils

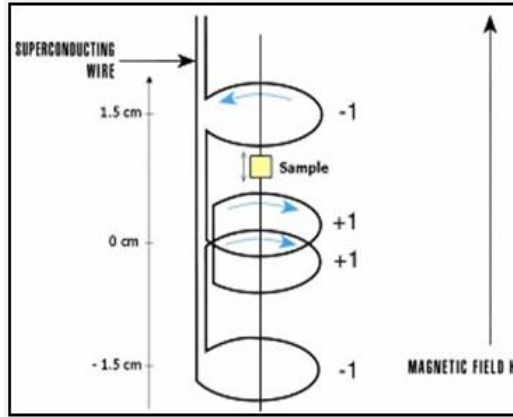


Figure 2.5: *Superconducting pick up coil diagram. Sample is kept at center of this coil. [37]*

due to change in flux because of sample. This current in the loop is connected to the input of Superconducting quantum interference device (SQUID) which converts it to a output voltage using superconducting junctions called Josephson junction. This output voltage is converted to magnetic moment using a calibrated system. As Squid is very sensitive to small currents due to changes in magnetic field, it is used for accurate and precise measurements.

Quantum Design MPMS XL is used for all the magnetization measurements done in this project. MPMS XL can go up to 7 Tesla magnetic field and can measure up to 10^{-6} emu. Magnetization and remanence measurements were done by following a particular sequence. In this sequence, a constant magnetic field was applied and the sample was cooled from 300K to 5K while taking magnetization data. Now the field was switched off and magnetization measurements were made while heating the sample from 5K to 300K and this is referred to as Thermo-Remnant Magnetization measurement (TRM).

2.7 Magnetoresistance measurement in PPMS

Physical property measurement system (PPMS) Ever Cool 2 is an analytical instrument by quantum design which can measure DC and AC resistivity, Hall coefficient, I-V curve, heat capacity with controlled temperature and magnetic field for samples. In this project, DC resistivity measurements were done by varying temperature from 300K to 5K. For DC resistivity measurements, powdered sample was pelletized and cut down into a rectangular shape. This rectangular pelletized cut was loaded onto a puck. Four probe resistivity

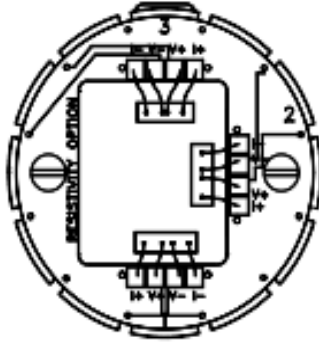


Figure 2.6: *Illustration of a puck with 3 samples, each having 4 contacts for resistivity measurement. [38]*

measurements were made by connecting four copper or gold leads from puck electrodes to the sample [fig 2.6]. Four probe resistivity measurements are necessary for low resistance samples as it eliminates the leads and contact resistance using separate probe for current sourcing and voltage sensing. By sourcing current from outer leads and sensing voltage from inner leads PPMS gets resistance value which can be converted to resistivity value using the equation 2.2 and measuring the values of length between voltage leads and area of cross section.

$$R = \frac{\rho L}{A} \quad (2.2)$$

where R= Resistance, ρ = Resistivity, L= Length between 2 voltage leads, A= Area of cross section.

2.8 Probe station

Probe station is an instrument mainly used for device characterization, I-V measurements and capacitance measurements. In this instrument, 4 gold probes (needles) with varying tip diameter from 200nm-20 μ m can be placed on a desired part of a device/sample with help of micro-manipulators which can move the probe by micron size in all three dimensions. The sample is place on a stage and a microscope is positioned above the stage to be used for imaging purpose. The whole assembly is built to have isolation from

vibrations and external light to reduce any external stimuli to the system and remove erroneous contribution to signal. The micro-manipulator and probe assembly is connected to Source Measure Unit (SMU) which is used to source or measure both current and voltage. An assembled probe station from Precise measurement technologies and 4200 Semiconductor Characterization System by Keithley was used for I-V measurements in four probes geometry.

Chapter 3

Synthesis, Characterization and magnetic measurements of bulk and 2D SrRu_2O_6

3.1 Sample Preparation and Characterization

Polycrystalline sample of SrRu_2O_6 was synthesized using hydrothermal method. In this method, stoichiometric ratio 2:1 of KRuO_4 (Alfa Aesar, 98%) and SrO_2 (Sigma, 98%) respectively was added to desired amount of distilled water [29]. Adding KRuO_4 to water+ SrO_2 mixture gave a reddish-brown colour which quickly turned black after 10 minutes of stirring. This mixture was heated at 200°C for 24 hours in 45ml Teflon lined steel autoclave. Precipitate was recovered using vacuum filtration assembly and washed with dil. HCl, distilled water and acetone. Parameters and results of all trials is given in figure 3.1 where it can be seen that the 2nd trial was most successful. The hydrothermal autoclave assembly was obtained from Parr instrument company.

Powder X-ray diffraction data at room temperature on prepared sample of SrRu_2O_6 is shown in fig 3.1. Peaks are indexed with SrRu_2O_6 and RuO_2 phases from the reported data in [29] and JCPDS[65-2824]. RuO_2 impurity phase is small as compared to SrRu_2O_6 and highest intensity peak ratio between them is 1:30.

SEM image of SrRu_2O_6 sample is shown in fig 3.2. Crystals of hexagonal shape and

Trial No	Concentration of KRuO ₄ (mmol)	Concentration of SrO ₂ (mmol)	Amount of water (ml)	Product obtained
1	2	1	20	Mostly Ru metal
2	3	1.5	32	SrRu ₂ O ₆ (90%), RuO ₂ (10%)
3	2.6	1.3	32	Compound destroyed due to use of Conc HCl while washing.
4	1.5	0.75	32	SrRu ₂ O ₆ (50 %), RuO ₂ (50 %)

Table 3.1: *Parameters for synthesis of SrRu₂O₆ with Hydrothermal method.*

mesoscopic size can be seen in this figure. It can also be observed that one crystal is clearly composed of many stacked layers. The hexagonal morphology of the grain could be the result of inherent hexagonal symmetry in SrRu₂O₆ and the layers observed in this crystal could be because of the internal layered structure in the compound. The presence of smaller particles over the hexagonal crystal is attributed to RuO₂ impurity. EDAX method is used to analyse the elemental composition of this compound. Total 4 crystals were selected and EDAX measurements on 8-9 points in each crystal was performed for statistical significance. The ratio for Sr:Ru was found to be 0.94:2 which is within the acceptable limit of the ideal case of 1:2.

Raman spectroscopy instrument with 50X magnification lens and $\sim 5 \mu\text{m}$ laser line width is used. Crystals of SrRu₂O₆ compound are in mesoscopic size and hence raman spectra over one single crystal was possible to obtain. First principles calculation study on this compound has been reported and suggests that SrRu₂O₆ correspond to one of the cleanest formed molecular orbitals [39]. Experimental Raman spectra over this compound is not reported in literature and therefore in order to confirm the result, spectra over 15 different single crystals were repeated to obtain statistically significant data. Raman spectra over a single crystal is shown in the figure 3.3. Peaks were obtained at raman shift of 204.19, 313.51, 510.51, 564.03, 631.79 cm⁻¹ and a broad peak from 360.3 to 414.86 cm⁻¹ maximizing at 384.11 cm⁻¹. The ratio between 204.19 and 313.79 cm⁻¹ is calculated for all spectra taken over 15 single crystal and the average was found out to be 1:0.28. Iso-structural compound of SrRu₂O₆ is PbSb₂O₆ and hence, phonon peak in Raman spectra, which correspond to lattice vibration, should be at similar Raman shift position for both of them. Lattice peaks for PbSb₂O₆ is found out to be 210 cm⁻¹ and

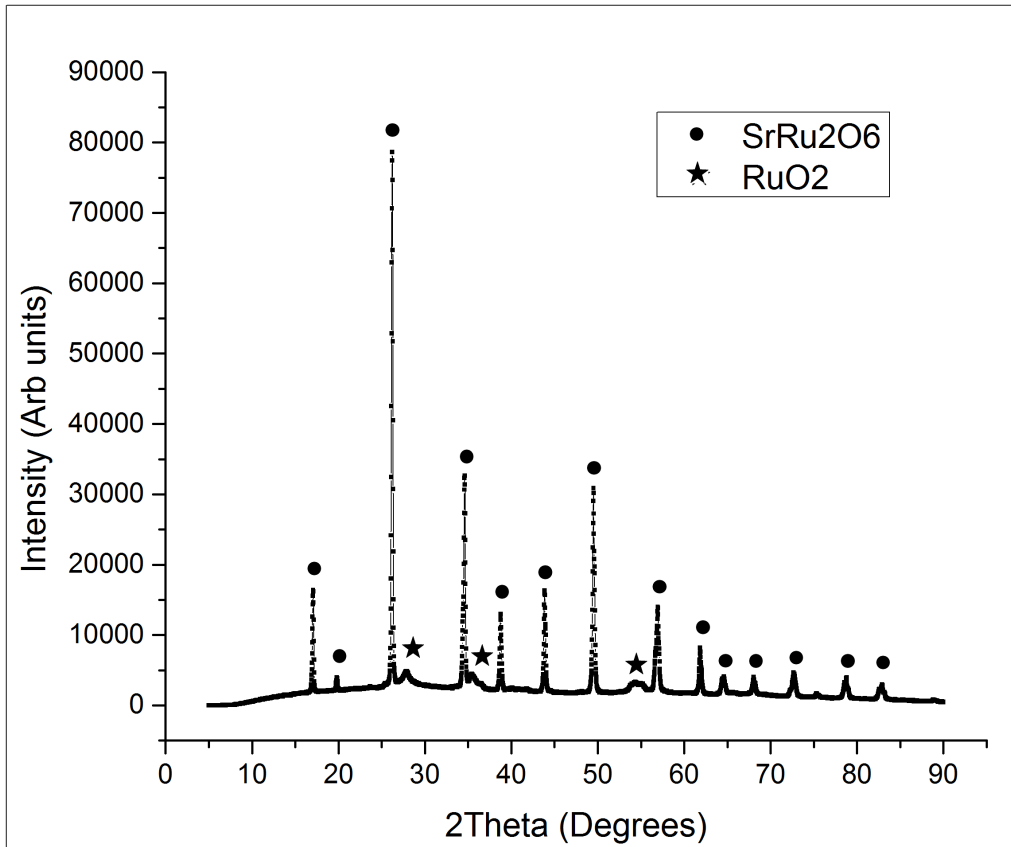


Figure 3.1: Powder XRD data showing SrRu_2O_6 and RuO_2 phase

655 cm^{-1} [40] which could roughly correspond to 204.19 and 631.79 cm^{-1} in SrRu_2O_6 .

3.2 Magnetic measurements

Magnetic measurements on SrRu_2O_6 were performed in SQUID. Magnetization data was obtained while cooling the sample from 300 K to 5K under a magnetic field of 5000 Oe. An upturn in the magnetization data below ~ 150 K can be clearly seen from figure 3.4. This upturn is attributed to RuO_2 impurity in the sample by comparing it with the reported data for RuO_2 [41]. As the transition temperature of SrRu_2O_6 is 575 K [27], we need high temperature magnetization data to verify the transition. The flat curve from 150 K to 300 K is in agreement with the SrRu_2O_6 data in [29].

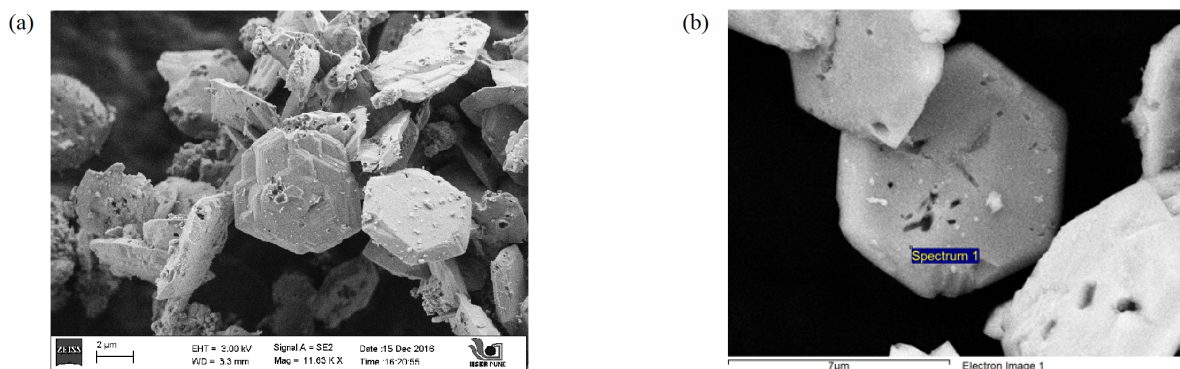


Figure 3.2: SEM Images of SrRu₂O₆. (a) Layered hexagonal crystals of the compound. (b) EDAX marker over a single hexagonal crystal.

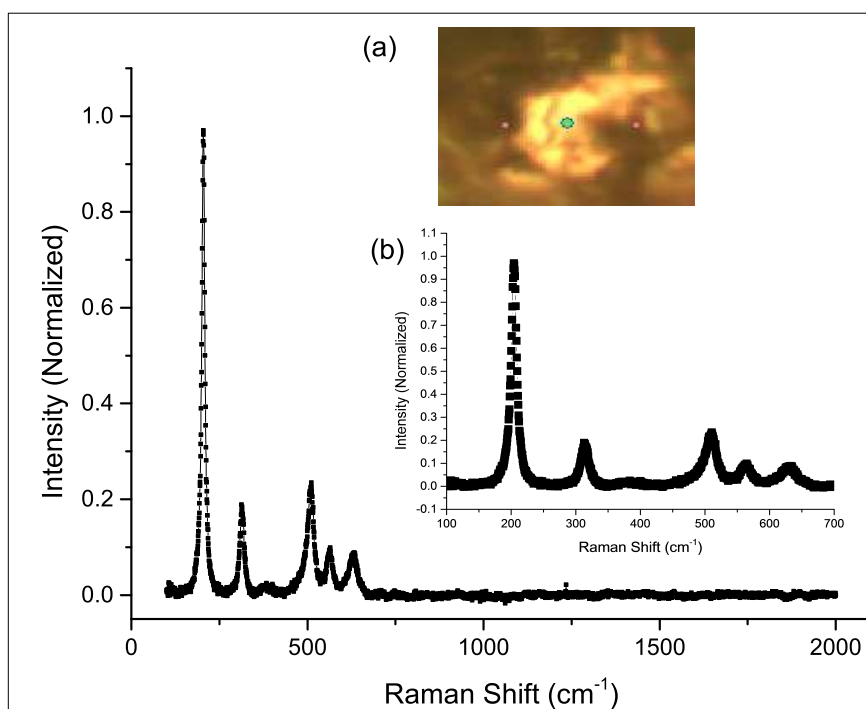


Figure 3.3: Raman spectra of a single crystal SrRu₂O₆. (a) Upper inset shows Raman pointer on a single hexagonal crystal. (b) Lower inset shows zoomed in spectra from 100-700 cm⁻¹

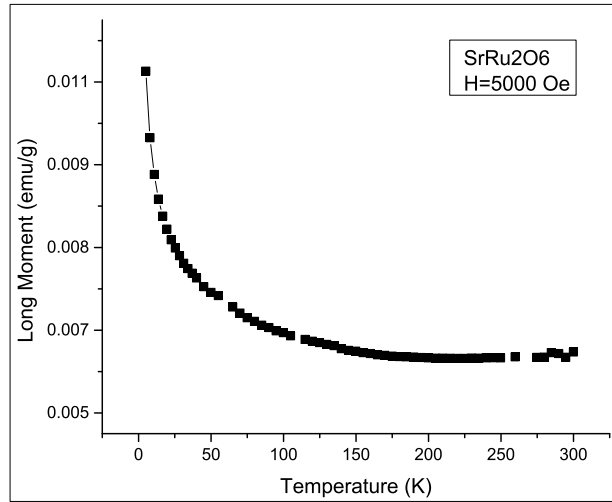


Figure 3.4: Magnetization vs Temperature data of SrRu_2O_6 at 5000 Oe.

After cooling down to 5K, the magnetic field was switched off and magnetization data was taken while heating the sample from 5K to 300K. The remanence magnetization obtained by this protocol is called Thermo-Remnant Magnetization (TRM). TRM measurements for SrRu_2O_6 is shown in figure 3.5. Remanence magnetization with temperature evolution in TRM data could indicate magneto-strictive effects in SrRu_2O_6 system. Magnetostriction causes change in magnetic moments due to modulation in lattice parameters and such modulation of c axis with change in temperature is indeed found in SrRu_2O_6 [27]. Comparing M-T data with TRM data we found that, magnetization value in 5000 Oe field at 11K is 96.25×10^{-4} emu/g and remanence magnetization after switching the field off at 11K is 4.27×10^{-4} emu/g. Therefore, 4.43% magnetization is retained after switching the field off.

3.3 Liquid exfoliation

It can be seen in fig.3.2 that SrRu_2O_6 crystal have multiple layers stacked one over the other. An attempt is made to separate these layers into 2D sheets through the method of liquid exfoliation. Process of exfoliation and characterization of the exfoliated sheets is presented in this section.

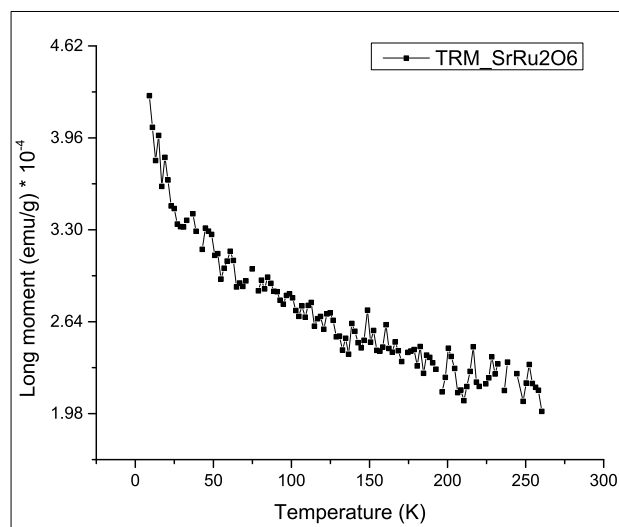


Figure 3.5: TRM vs Temperature measurements of SrRu_2O_6 , at cooling field of 5000Oe.

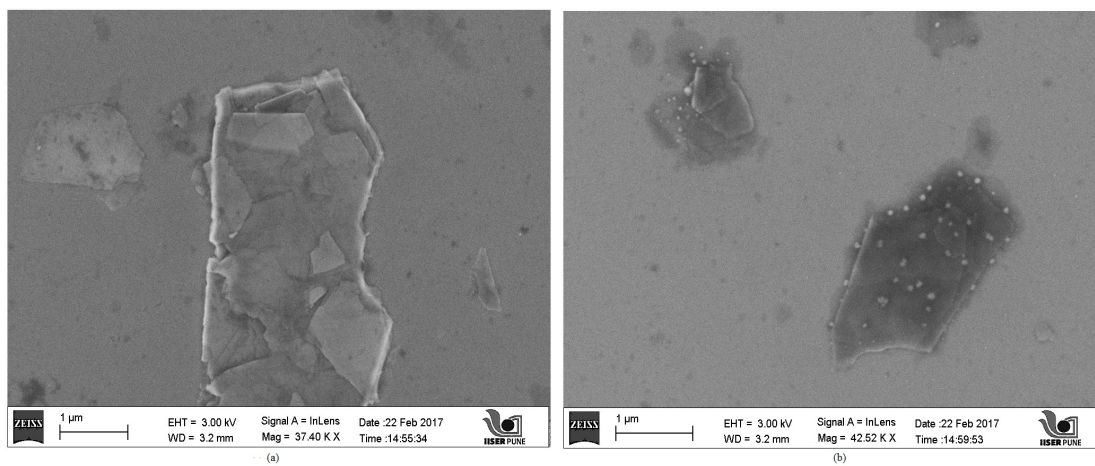


Figure 3.6: SEM image showing exfoliated sheets of SrRu_2O_6 in InLens mode.

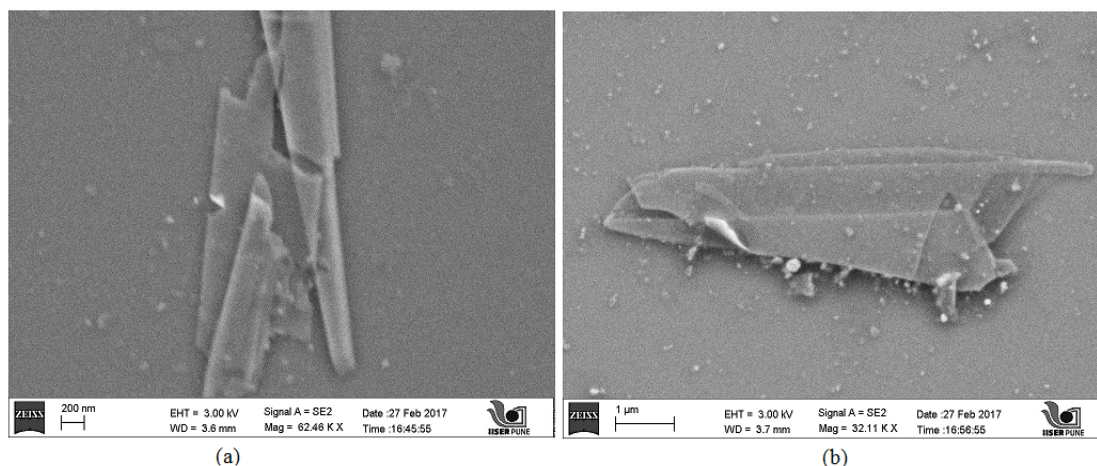


Figure 3.7: SEM image showing exfoliated sheets of SrRu_2O_6 in SE2.

3.3.1 Bulk exfoliation

SrRu_2O_6 sample of 3mg was suspended in 30ml ethanol solvent kept in 100 ml glass beaker. Sample was sonicated using bath sonicator for 4 Hrs and probe sonicator for another 4 Hrs. After the sonication procedure, sample was kept undisturbed for a whole day to let the sample reach a equilibrium state. The top part of the settling suspension was collected in a centrifuge tube and was centrifuged at 2000 RPM for 30 minutes. Centrifugation causes a layer wise gradient distribution of size and mass in the centrifuge tube and as 2D flakes are low mass objects, they are expected to occupy the top layer after centrifugation. About $5 \mu\text{L}$ of sample was taken from top layers of centrifuge tube and drop casted onto a silicon wafer to image in SEM instrument. Image in figure 3.6 (a) shows a bulk crystal with sheets of $\sim 1\text{-}2\mu\text{m}$ in process of separation from it. In figure 3.6 (b), separated sheet with possibly RuO_2 impurity on its surface can be seen which hints that this layer is separated from top layer of bulk crystal which also had RuO_2 impurity. Figure 3.7 was taken in SE2 mode which shows enhanced topographical information than Inlens mode and in this image, thin sheets can be seen and multiple layered sheets can be identified. Therefore, at first instance it can be seen that the exfoliation of SrRu_2O_6 seem possible and due to liquid exfoliation technique, high yield was obtained. Further optimization of parameters is required to obtain single layer sheets.

3.3.2 Raman spectroscopy

Literature on Raman spectroscopy suggests that there is shift in Raman peaks between 3D bulk material and 2D exfoliated analogue. This shift in peaks is related to the absence or reduction of interlayer vibrational contributions to the spectra in 2D material as compared

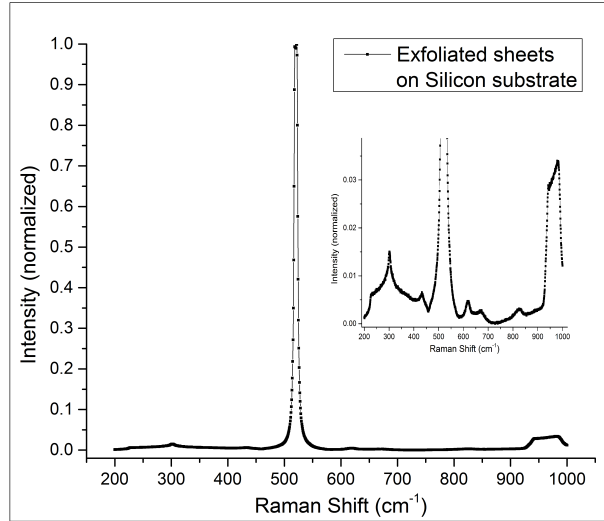


Figure 3.8: Figure showing Raman spectra of exfoliated sheets of SrRu_2O_6 on Si substrate. Inset shows enlarged image of spectra giving information about lower intensity peaks.

to 3D. In order to verify if the sheet like structure seen in figure 3.6 is 2D material, Raman spectra of these sheets drop casted over Silicon wafer was obtained.

It can be seen in normalized Raman spectra figure 3.8, a major peak of silicon at 520.7 cm^{-1} and plateau region from 940 cm^{-1} to 980 cm^{-1} appears. Apart from these two major peaks, many peaks are seen after zooming in as seen in inset of figure 3.8. The kink at 230 cm^{-1} and peaks at $303, 435, 460 \text{ cm}^{-1}$ are associated to acoustic phonon modes [42] of Silicon. We know from figure 3.3 that peaks of bulk raman spectrum of SrRu_2O_6 are $204.19, 313.51, 384.11, 510.51, 564.03, 631.79 \text{ cm}^{-1}$ and hence we should expect shift of these wavenumbers in 2D Raman spectrum. But as the expected position of 2D peaks and those of Si peaks are very close, we would have to use analytical methods to fit the peaks in the graph and distinguish between them. Possibility of using other substrates instead of silicon is being explored.

Chapter 4

Magnetic measurements and Exfoliation of Na_2IrO_3

4.1 Sample Characterization

Single crystals of Na_2IrO_3 were provided by Dr. Yogesh Singh from IISER Mohali. Characteristics of this single crystal can be seen in [30]. I-V measurements and Raman spectroscopy over single crystals was performed and is presented in this section.

4.1.1 Raman Spectroscopy

Raman spectra of Na_2IrO_3 single crystal using 488 nm laser as excitation wavelength is shown in figure 4.1. Raman peaks can be observed at 213.4, 285.5, 384.3, 460.1, 493.5, 569.3 and 627.5 cm^{-1} raman shift. Peaks at 460.1, 493.5 and 569.3 cm^{-1} are identified as Bg(1), Bg(2) and Ag respectively [32]. This Raman spectra for bulk Na_2IrO_3 in 488nm laser serves as reference for further experiments.

4.1.2 I-V characterization

Probe station was used to make four probe I-V measurements on single crystal Na_2IrO_3 kept on silicon substrate which was fixed with glass slide for stability. Four probe technique was used to reduce the additional resistance sources due to contact between probes and material. Gold plated tungsten probe of 5 μm tip diameter was positioned over the sample with help of micromanipulators and microscope. The image in figure 4.2 shows 4

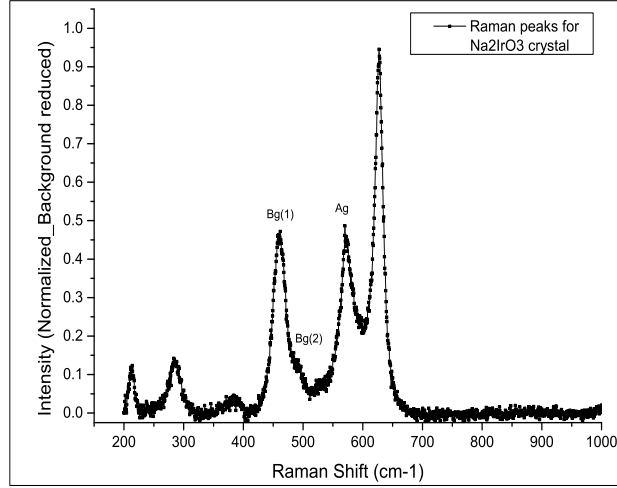


Figure 4.1: Raman spectra for single crystal Na_2IrO_3 using 488nm laser .

tips touching the Na_2IrO_3 single crystal. Probes 1,4 are used for sourcing current and 2,3 for voltage sensing. The dimensions of crystal was measured using a calibrated length scale system. In this system, magnification strength was associated with a specific scale using a already known length scale system as a reference. Thickness of $100 \mu\text{m}$ is assumed [30] and breadth is measured to be $\sim 800 \mu\text{m}$. Length between 2 voltage probes is $340 \mu\text{m}$.

I-V measurements were made using 4200 SCS semiconductor characterization system. Voltage difference between two voltage probes was measured by sourcing current from $\pm 4\text{mA}$ with 0.1mA step. The graphs showing separate I-V curves from -4mA to 4mA and -1mA to 1mA is given in figure 4.3. A slight non linear pattern is observed in I-V scans limited to $\pm 4\text{mA}$, as shown in figure 4.3(a). Linear pattern is observed for I-V upto $\pm 1\text{mA}$ and slope for this straight line gives resistance value of 895.56Ω which can be converted to resistivity value using the formula 4.1.

$$R = \frac{\rho L}{A} \quad (4.1)$$

The resistivity value obtained for Na_2IrO_3 using this formula is $21.15 \Omega \text{ cm}$ which is in agreement with reported value near room temperature [30]. Slight variation could be due to the resistive heating effect occurring by passage of current in the sample.

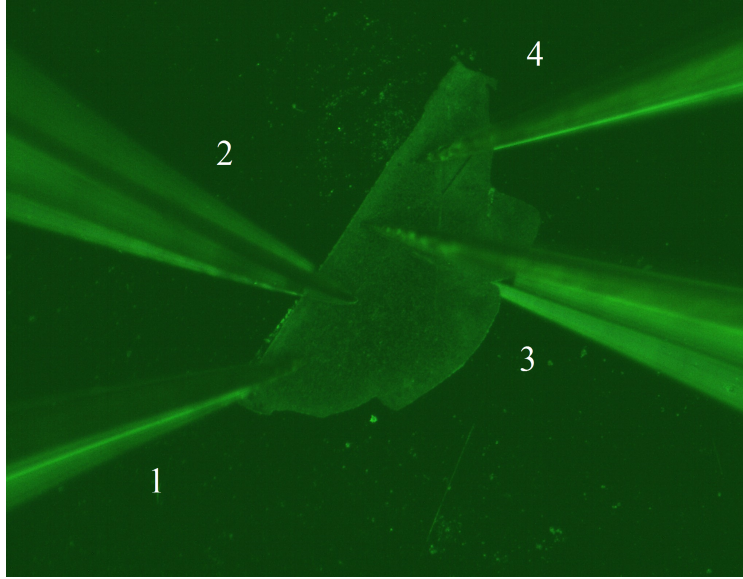


Figure 4.2: Set-up of four probes touching the surface of single crystal for I-V measurement.

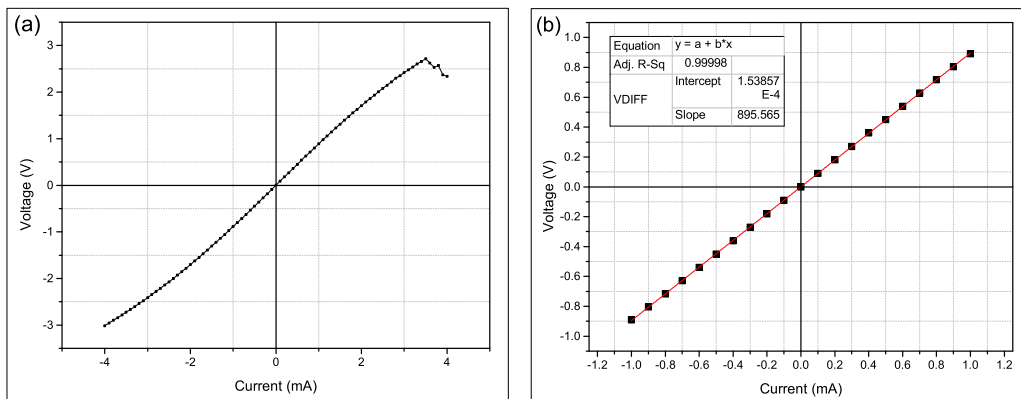


Figure 4.3: I-V curve for Na_2IrO_3 . (a) Graph from -10mA to 10 mA. (b) Graph from -1mA to 1mA.

4.2 Magnetic measurements

Randomly oriented single crystals of Na_2IrO_3 were packed in capsule tube and loaded in MPMS for magnetic property investigation. Magnetization (M) vs Temperature (T), TRM vs T and M vs Magnetic field (H) experiments were performed. M vs T measurement was made by measuring magnetic moment while cooling the sample in 1000 Oe magnetic field. Graph showing M vs T can be seen in figure 4.4 (a). Paramagnetic

behaviour is seen from the graph and inverse susceptibility vs temperature was plotted in 4.4 (b) to fit Curie-Weiss (CW) equation 4.2 and check for any deviations from Curie-Weiss behaviour. It is evident from the fit that there is clear deviation from Curie-Weiss behaviour starting from 110K. Slope of this linear fit gives us the value of Curie constant $C = 1.721$ and knowing the value of intercept and C gives us the Curie temperature $\theta = -112$ K. The value of Curie temperature is in agreement with the reported value [30].

The sample is chemically unstable and degrades if exposed to air for a longer period of time [43]. Although the sample was kept in tight vacuum, it was necessary to confirm if it is still intact. Here the standard magnetization data was used to confirm this and the agreement between the reported and our data shows that the sample is still intact. The magnetization data is given in [43] for the sample which was exposed to air and hence got degraded.

$$\chi = \frac{C}{(T - \theta)} \quad (4.2)$$

The deviation of plot from CW behaviour below 110K and the Curie temperature of 112K which is much higher than experimental confirmation of antiferromagnetic transition at 15K is attributed to the existence of magnetic correlations much above transition temperature [30].

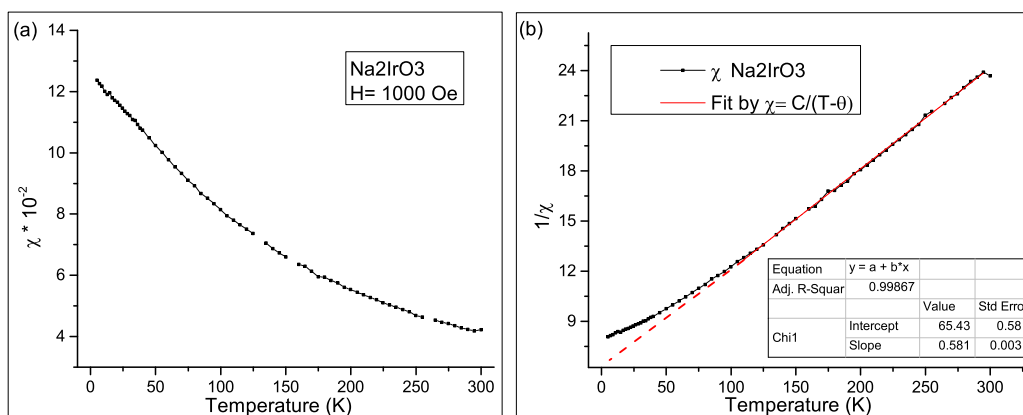


Figure 4.4: (a) Magnetic susceptibility versus temperature graph for Na_2IrO_3 . (b) Inverse susceptibility ($1/\chi$) versus T plot for Na_2IrO_3 . Red line shows Curie Weiss (CW) fit

The magnetic field was switched off at 5K and the temperature variation of remanence in heating cycle was measured. The figure 4.5 shows the TRM data and finite remanence

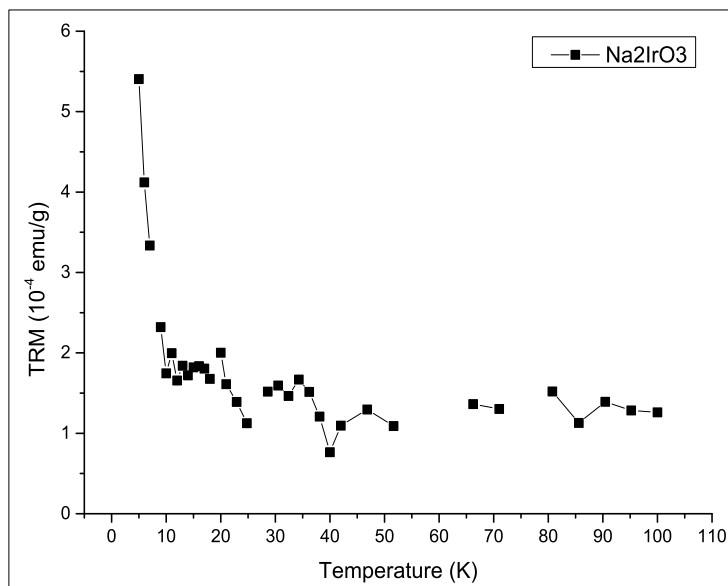


Figure 4.5: Plot of TRM vs Temperature for Na_2IrO_3 . Gaps in the plot is due to removal of bad data points.

in this systems suggests existence of magneto-strictive effects in this compound. It can be seen that TRM drops significantly around 12 K and this could be due to the transition of Na_2IrO_3 from antiferromagnetic long range ordering to weak magnetic correlation state at 15 K. Comparing M-T data with TRM data we found that, magnetization value in 1000 Oe field at 5K is $123.7 * 10^{-4}$ emu/g and remanence magnetization after switching the field off at 5K is $5.4 * 10^{-4}$ emu/g. Therefore 4.36% magnetization is retained after switching the field off. Also there is a sharp decrease in TRM from $5.4 * 10^{-4}$ emu/g at 5K to $1.74 * 10^{-4}$ emu/g at 10K. Only one set of TRM data is taken and field dependence TRM measurements are required to prove the existence of magnetostrictive effect. These measurements are planned in future.

The % TRM retained in SrRu_2O_6 sample is 4.43% at 11K after cooling the sample at 5000Oe and % TRM in Na_2IrO_3 sample is 4.36% at 5K after cooling the sample at 1000Oe.

4.3 Liquid exfoliation

Single crystals of Na_2IrO_3 was successfully exfoliated into bulk quantity by using already calibrated conditions for exfoliation. Bath sonication for 2 hours and probe sonication for

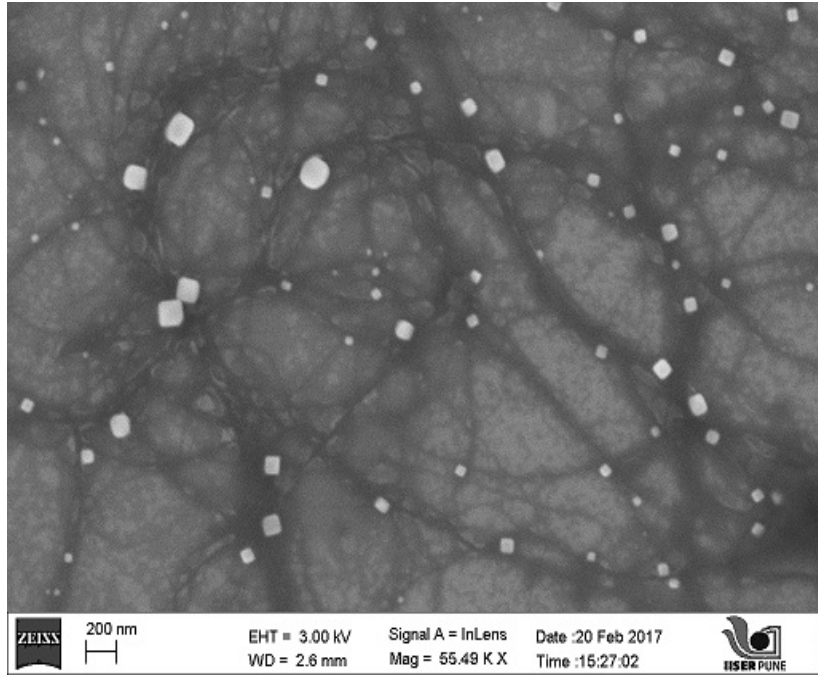


Figure 4.6: Figure shows SEM image of rectangular flakes Na_2IrO_3 obtained from bulk exfoliation.

3 hrs was done for 1 mg sample in 75 ml ethanol. The size of the flakes as seen in SEM figure 4.6 is ~ 200 nm with square shape morphology. Number of attempts to increase the size of the flakes were made, however it did not lead to increase in size. AFM image and Raman spectra of these sheets is needed in order to confirm that these are in fact 2D sheets. One of the primary aim is to conduct magnetic investigations over this 2D sheets and hence significant number of sheets are required so as to gather enough weight for all magnetic measurements. For confirmation through Raman spectroscopy these sheets are drop casted over Si wafer but as the expected peaks for Na_2IrO_3 4.1 lie close to the Si peaks 3.8, it is difficult to differentiate both. Therefore Raman spectra of 2D flakes over different substrate has to be done and currently such substrate with no coinciding peaks with Na_2IrO_3 is being searched upon.

Chapter 5

Magnetoresistance measurements in Ni-NiO system

5.1 Sample Characterization

Nickel (Ni) samples with hexagonal plate, rod-like and spherical shape morphology were synthesized using standard solution chemistry/wet chemistry route and hydrothermal method. In a typical sample synthesis with solution chemistry route, stoichiometric amounts of Nickel Sulphate ($\text{NiSO}_4 \cdot x\text{H}_2\text{O}$) and Sodium Hydroxide (NaOH) were added in distilled water or ethylene glycol solution at 60-70° C and the resulting nickel hydroxide ($\text{Ni}(\text{OH})_2$) is reduced at desired temperature using hydrazine hydrate, to obtain Ni precipitate. Magnetic filtration was done to collect the Ni precipitate after washing it vigorously with distilled water, ethanol and acetone. By varying parameters like concentration of NaOH, NiSO_4 and solvent, we have prepared Ni samples with morphologies of Hexagonal plate, spherical and rodlike shape as can be seen in table 5.1. SEM, pXRD and schematic representation for formation of these systems is given in figure 5.1,5.2,5.3. A thin Nickel Oxide (NiO) layer is naturally grown over Ni due to surface reactivity of Ni with oxygen molecule. The existence of NiO in all these materials is evident from the Raman spectra 5.5.

Nickel samples with thin sheets morphology of larger size and higher crystallinity were synthesized using hydrothermal synthesis method. In this method, commensurate quantity of $\text{NiSO}_4 \cdot 6\text{H}_2\text{O}$ and NaOH materials mentioned in 5.1 were dissolved and mixed in 40ml ethylene glycol solution to form $\text{Ni}(\text{OH})_2$. This mixture was then poured into a

Concentration of NaOH (mmol/dm ³)	Concentration of NiSO ₄ .6H ₂ O (mmol/dm ³)	Solvent	Time for reduction (minutes)	Morphology	Size	Type of material
1.2	0.32	EG	90	Irregular	30-50 nm	Porous
2.5	0.32	EG	40	Irregular	30-50 nm	Porous
5.2	0.32	EG	5	Rodlike	500 nm	Porous
8.8	0.32	EG	1	Rodlike	2 μm	Porous
3.7	0.91	Water	10	Spherical	1 μm	Porous

Concentration of NaOH (mmol/dm ³)	Concentration of NiSO ₄ .7H ₂ O (mmol/dm ³)	Solvent	Time for reduction (minutes)	Morphology	Size	Type of material
7.7	1.8	Ethylene glycol (EG)	120 mins	Hexagonal plates	300-500 nm	Crystalline
7.7	1.8	Water	60 mins	Spherical	1 μm	Porous

Table 5.1: *Parameters for synthesis of Ni with distinct morphologies using solution chemistry route.*

Concentration of NaOH (mol/dm ³)	Concentration of NiSO ₄ .6H ₂ O (mol/dm ³)	Temperature (C)	Morphology	Size	Type of material
6.2	0.93	190	Spherical+rodlike	0.5-1 μm	Crystalline
12.6	0.93	190	Spherical+rodlike	0.5-1 μm	Crystalline
19.7	0.93	190	Thin sheets	1-1.5 μm	Crystalline
12.6	0.46	190	Thin sheets	0.5-1 μm	Crystalline

Table 5.2: *Parameters for synthesis of Ni with distinct morphologies using Hydrothermal method.*

Teflon lined cup which was kept inside an autoclave at 190°C for 3 Hours. Ethylene glycol at 190°C forms acetaldehyde which acts as a reducing agent and reduces Ni(OH)₂ to Ni. Sample was washed multiple times and was recovered using magnetic filtration. Samples with high crystallinity was obtained using hydrothermal method because of high pressure and high temperature generated inside Teflon lined cup. Hydrothermal reaction assembly was obtained from Parr instrument.

5.1.1 Hexagonal plates (HP)

The SEM image shows one over the other single crystal hexagonal plates of 300-500 nm dimension [see fig 5.1 (c)]. PXRD shows clear Ni peak with no impurity [5.1 (b)]. NiO layer peaks were not observed as total amount of NiO is not significant enough to contribute.

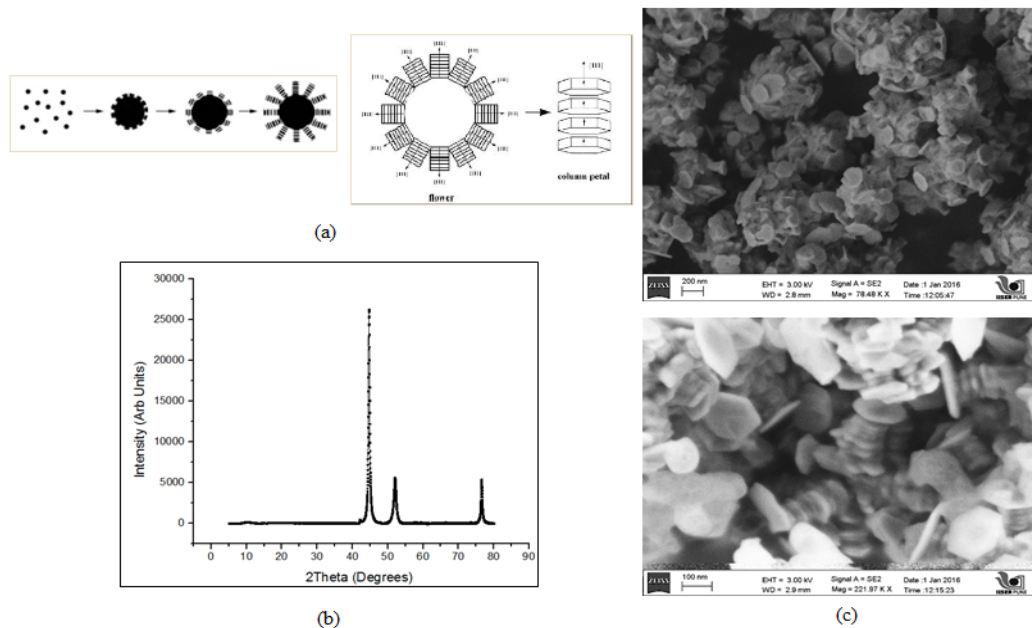


Figure 5.1: (a) Schematic of HP formation [44], (b) PXRD pattern of HP nickel (c) SEM image of HP

5.1.2 Rod-like particles

Micron sized rod-like particles can be seen in SEM image 5.2 (c). It is to be noted that these micron sized particles are not single crystals but formed due to coagulation of nanometer sized grains. Schematic in figure 5.2 (a) shows the formation of rod-like morphology due to accumulation of smaller grains. PXRD shows clear Ni peaks.

5.1.3 Spherical particles

Ni particles of spherical morphology can be seen in SEM image 5.3 (c). Similar to rodlike particles, these spherical particles are formed due to coagulation of nanometer sized grains. Schematic in figure 5.3 (a) shows the formation of spherical morphology.

5.1.4 Thin Sheets

Crystalline Ni particles of thin sheets morphology can be seen in SEM image 5.4 (b). Many sheets are intertwined to form the the structure. Schematic in figure 5.4 (a) shows the formation of such thin sheets morphology. PXRD shows clear Ni peaks with additional phase.

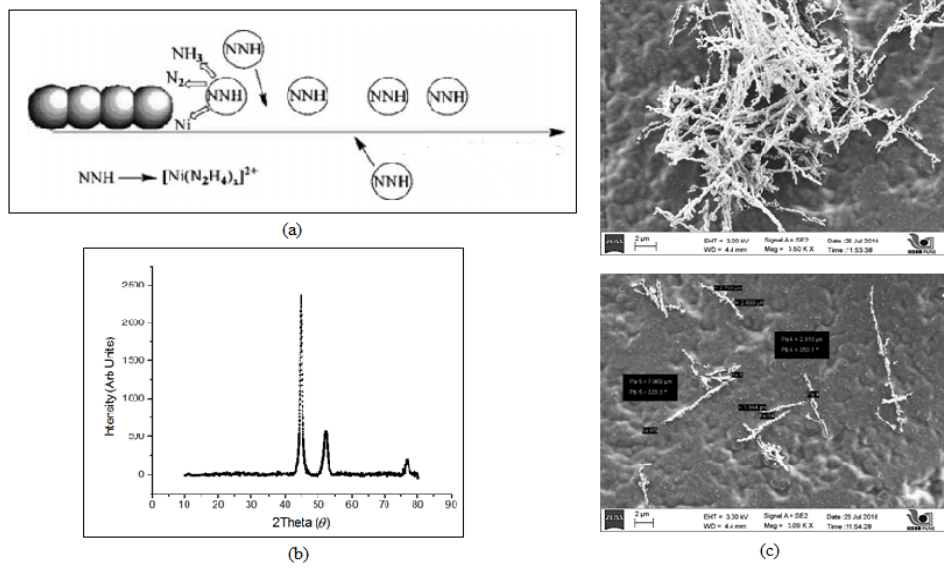


Figure 5.2: (a) Schematic of Rodlike formation [45], (b) PXRD pattern of rodlike nickel (c) SEM image of rodlike morphology.

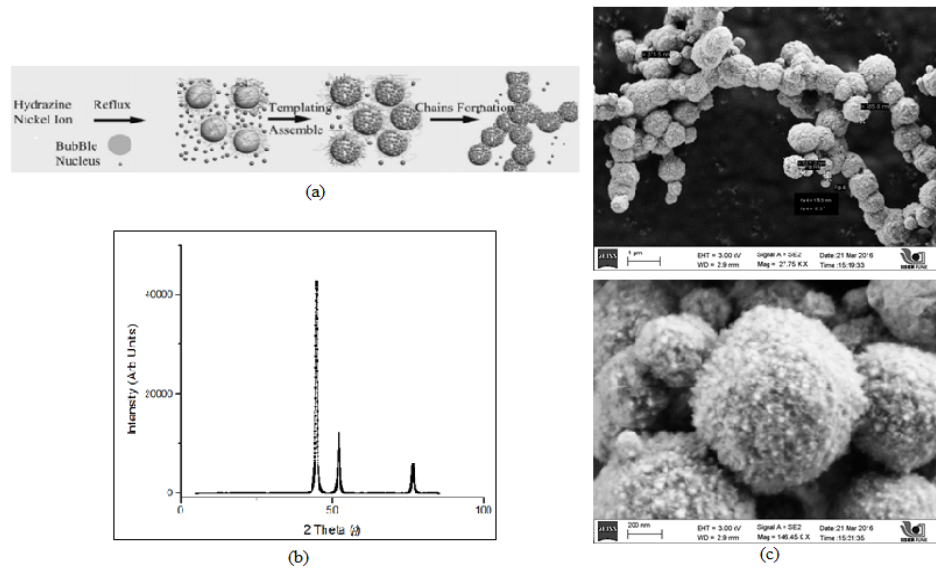


Figure 5.3: (a) Schematic of Spherical particle formation [45], (b) PXRD pattern of spherical nickel (c) SEM image of spherical morphology.

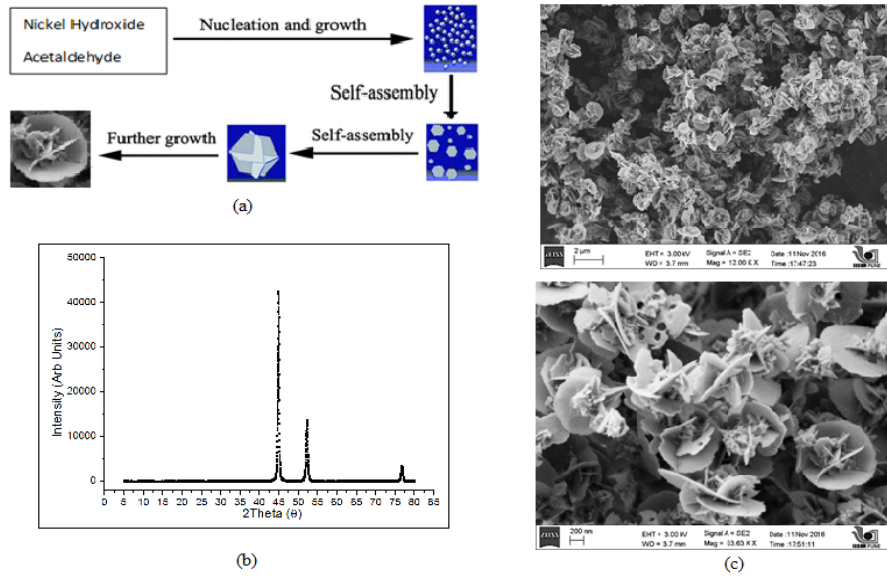


Figure 5.4: (a) Schematic of thin sheets formation [46], (b) PXRD pattern of thin sheets nickel (c) SEM image of thin sheets morphology.

5.1.5 Raman Spectroscopy

Raman spectroscopy is a surface sensitive technique and hence it was employed to experimentally validate the existence of naturally grown NiO layer over Ni. The spectra obtained using Raman spectroscopy on above mentioned morphologies in Ni system at 488nm laser wavelength is shown in figure 5.5 and also compared with standard NiO spectra at 532 nm laser wavelength obtained from [47]. The circular marked peaks in figures are phonon peak positions and as can be seen in figure 5.5, they agree well with standard NiO. Magnon peak is marked with a rectangular symbol in standard NiO and is absent in all samples. This absence of magnon peak could be due to very low thickness of NiO in the samples. This hypothesis is further supported by a study in [48] which show that the magnon peak intensity lowers drastically by decreasing the NiO size. Reason for Raman peak at around 300 cm^{-1} in samples marked with ? symbol has not been understood yet, but is suspected to be a characteristic of change in Raman excitation laser wavelength of 532 nm in standard NiO and 488 nm in these materials.

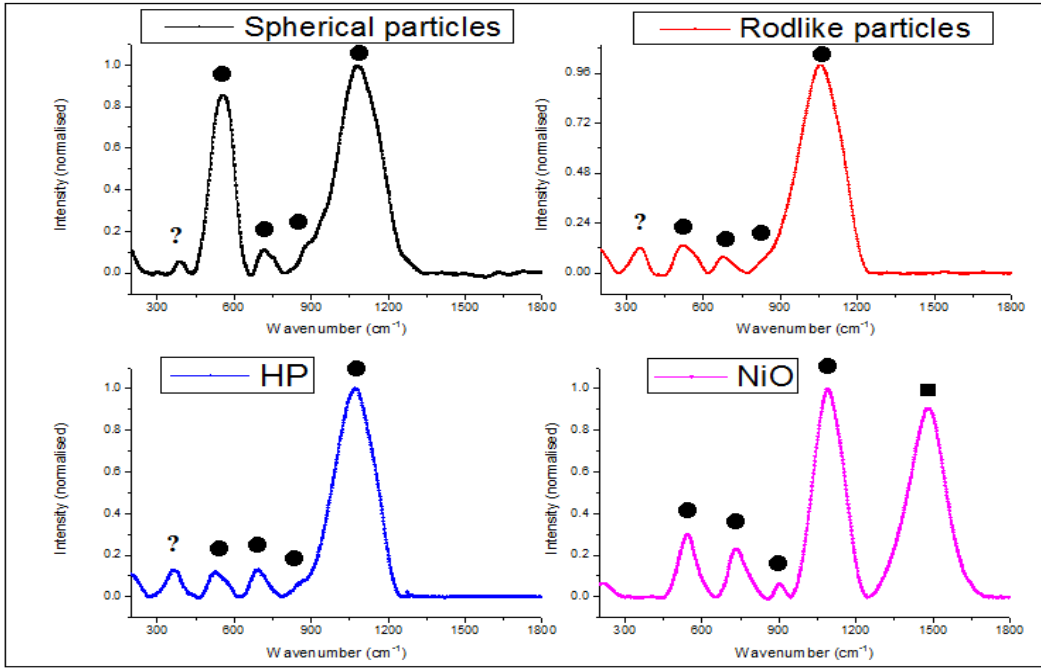


Figure 5.5: Raman spectra of samples with HP, rodlike, spherical morphologies and standard NiO. NiO phonon peaks are marked with circle.

5.2 Resistivity measurement

5.2.1 Effect of magnetic field

Standard four probe resistivity measurements over pelleted samples of above mentioned Ni-NiO systems. Resistivity measurements from 5K to 300K under the magnetic fields of 0 T (Tesla), 0.1 T and 1 T has been made. The figure 5.6 (a) shows temperature dependence of resistivity in all samples at 0T and a combination of metallic behaviour and activated behaviour is seen, although fitting the exact functional form is required to conclude. A peculiar anomaly can be seen in plot of HP samples at ~ 250 K. Figure 5.6 (b) also shows combination of metallic and activated behaviour in all samples at 0.1 T field and the anomaly in HP stays. Interestingly, this anomaly in HP sample vanishes at 1 T magnetic field as can be seen in figure 5.7 (a) and 5.7 (b). Similar transition in a closely related core-shell system of $\text{CrO}_2\text{-Cr}_2\text{O}_3$ is reported at ~ 250 K in [16] and therefore it is suspected that $\text{CrO}_2\text{-Cr}_2\text{O}_3$ and Ni-NiO HP sample could have similar dynamics at play.

The MR % vs Temperature at 0.1T and 1T magnetic fields is plotted in figure 5.8. MR of about -9% and -14% can be seen at 260K in 0.1T and 1T magnetic fields respectively.

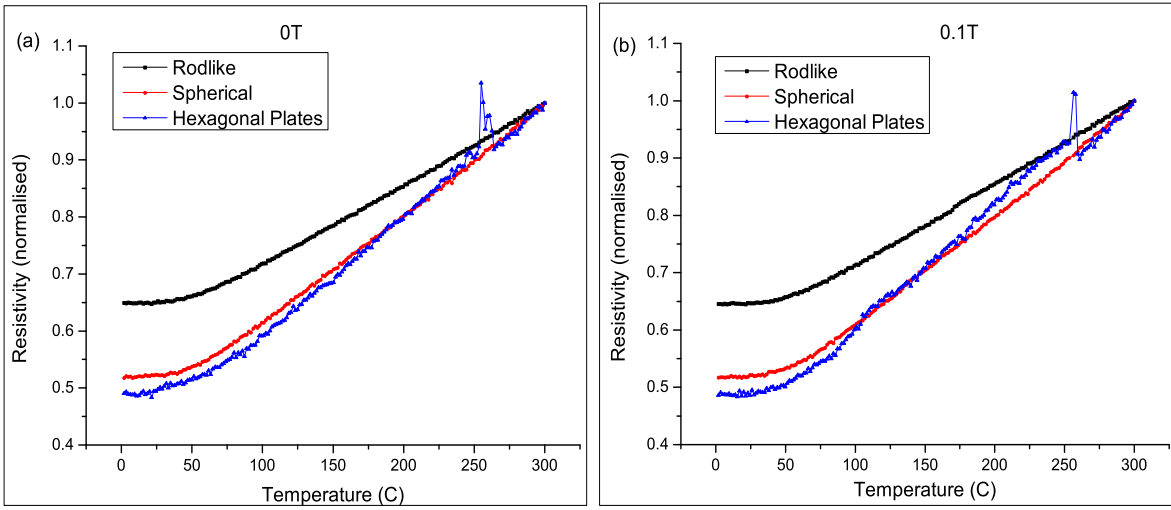


Figure 5.6: Resistivity vs Temperature plot for (a) 0T (b) 0.1 T magnetic fields

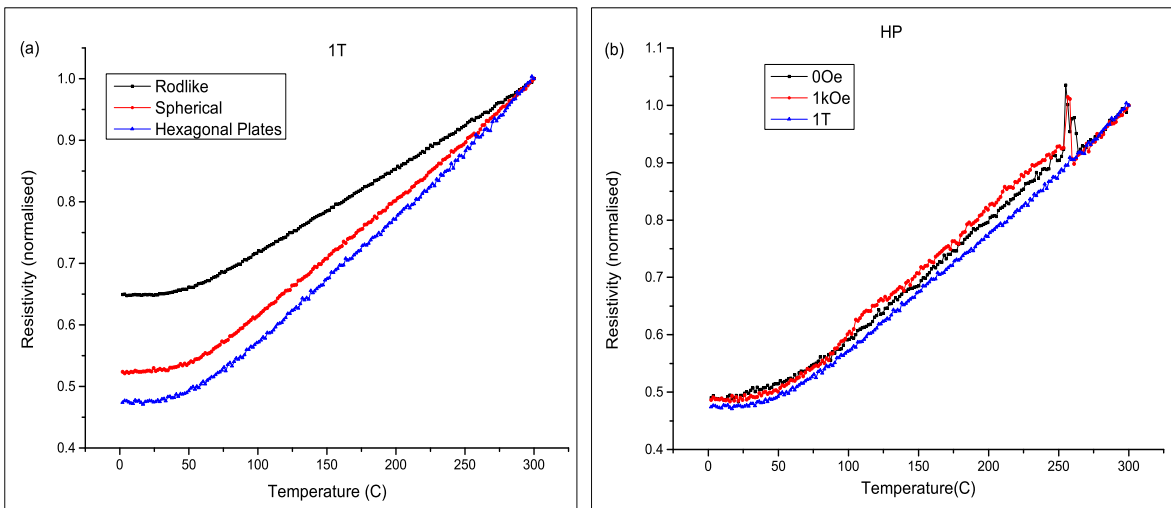


Figure 5.7: Resistivity vs Temperature plot for (a) 1T (b) only HP for 0T, 0.1T, 1T

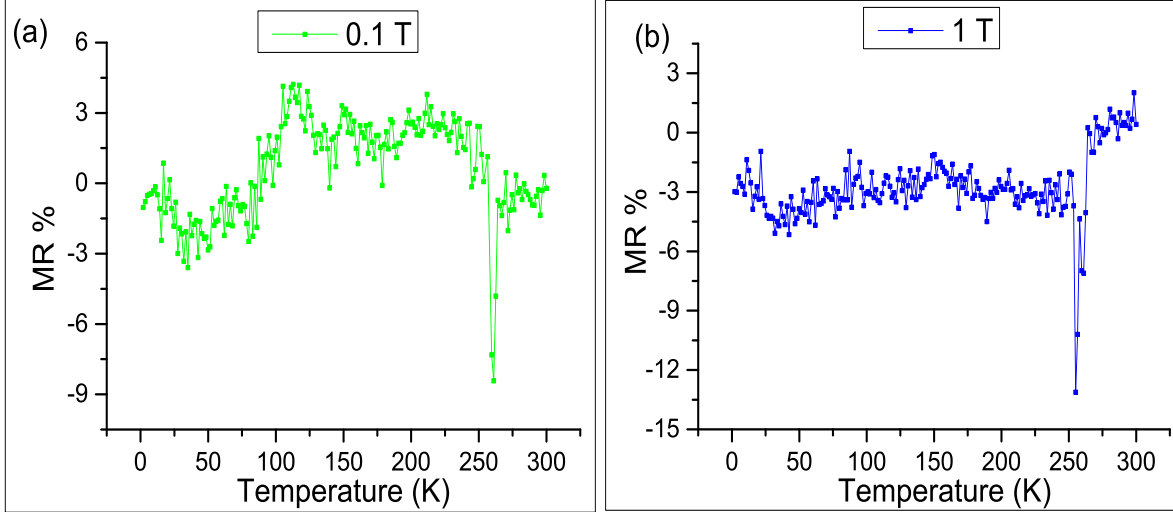


Figure 5.8: MR plots for (a) 0.1 T and (b) 1 T are shown

This is due to the anomaly seen at 250K in R vs T data. In MR plot for 1T field, an average MR of -3% is observed from 250K to 5K and goes to 0% from 270K to 300K. In MR plot for 0.1T field, a fluctuating MR from -3% to +3% is seen from 250K to 5K and settles down to 0% from 270K to 300K. The feature seen at 260K with sudden increase in MR could be due to magnetic interactions between ferromagnetic grain and antiferromagnetic grain boundary [16].

5.2.2 Effect of heating

It has been reported that the thickness of NiO layer can be modulated by heating the sample at different temperatures under varying O_2 pressure [49]. It is known that tunnelling phenomenon exponentially decreases with increasing barrier thickness [16]. To observe this effect, Ni-NiO spherical sample was heated at 200, 250, 300, 325, 350, 900 $^{\circ}C$ for 5 minutes at ambient oxygen pressure to increase NiO layer. PXRD shows increasing contribution of NiO at different temperatures in figure 5.9. Heating at 900 $^{\circ}C$ shows complete conversion of Ni to NiO. Four probe resistivity measurements of pelleted Ni-NiO sample heated at 325 and 350 $^{\circ}C$ is shown in figure 5.10. The plot for sample treated for 325 $^{\circ}C$ shows metallic behaviour whereas plot of 350 $^{\circ}$ treatment shows insulating behaviour. The barrier thickness in 350 $^{\circ}$ treatment could have exceeded the limit of thickness required for tunnelling, making NiO the main contributor to resistivity.

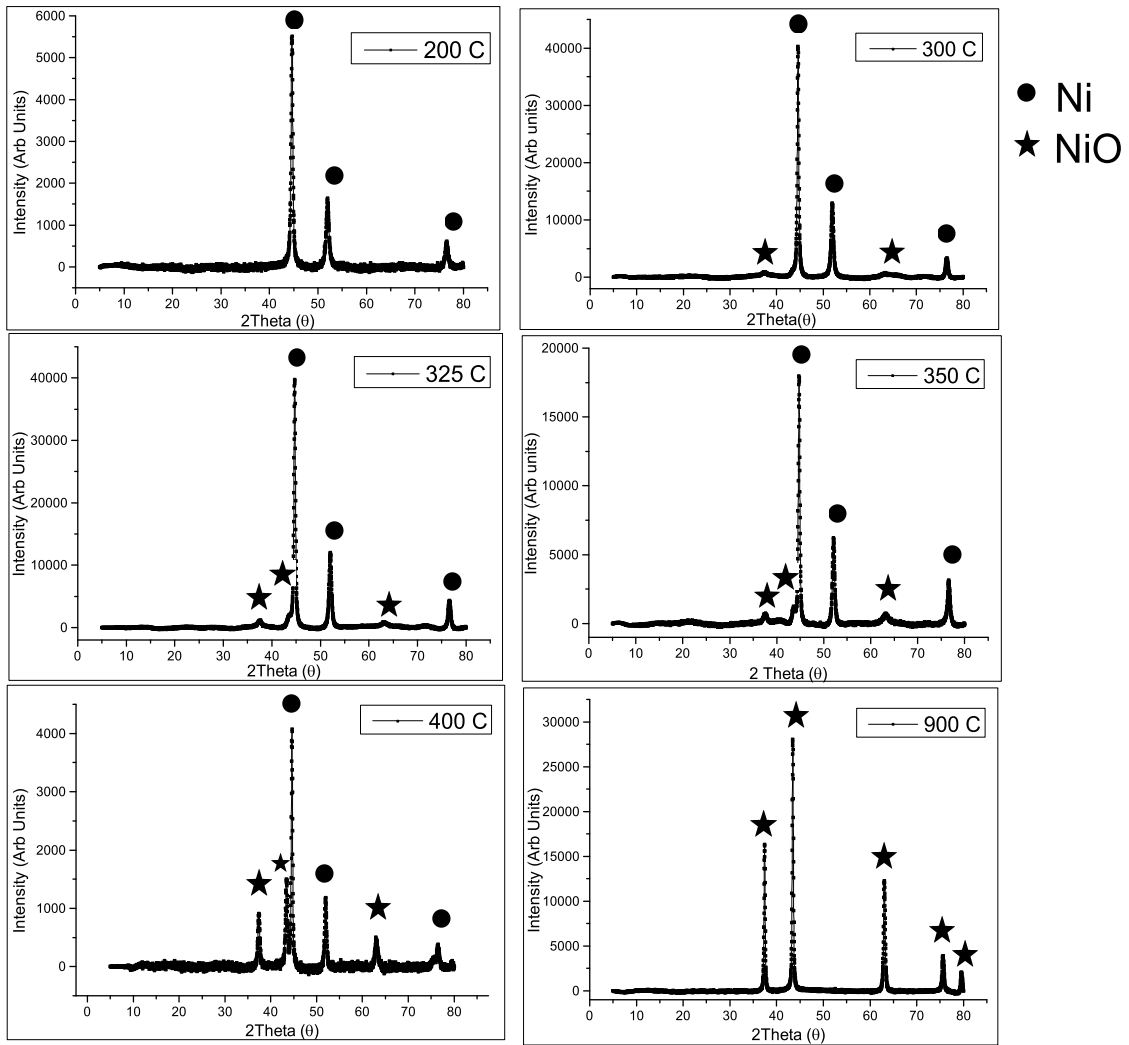


Figure 5.9: XRD plot for different heat treatment of spherical Ni-NiO samples.

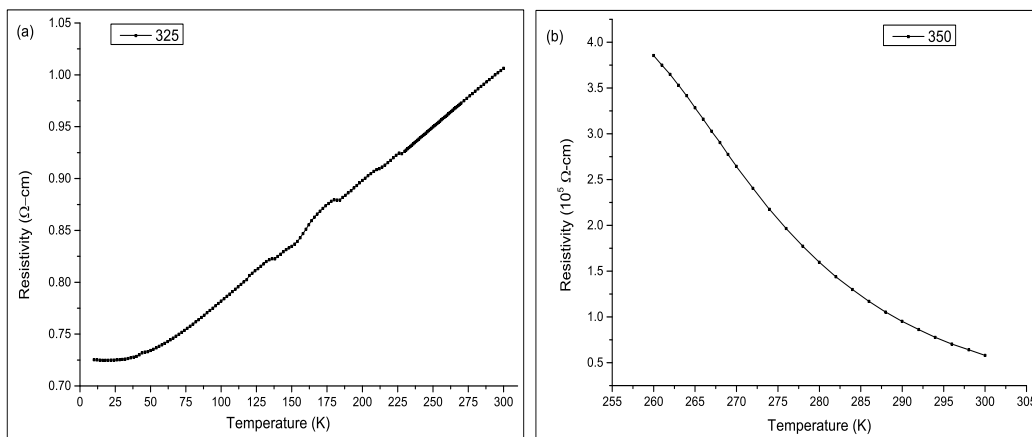


Figure 5.10: Resistivity versus Temperature at 0T field for spherical Ni-NiO sample heat treated at (a)325 (b)350

Chapter 6

Summary and Future work

6.1 Summary

Polycrystalline samples of SrRu_2O_6 and Ni-NiO were synthesized using solution chemistry and hydrothermal methods. Characterization of synthesized samples and Na_2IrO_3 sample (provided by Dr. Yogesh Singh) was made using XRD, SEM and Raman spectroscopy. Magnetic measurements on SrRu_2O_6 and Na_2IrO_3 was made and finite TRM was seen in both systems suggesting magneto-elastic coupling. Curie Weiss law fit for paramagnetic region of Na_2IrO_3 in M-T data predicted transition temperature much larger than experimentally observed T_N , this suggests magnetic interaction exists well above T_N . Magneto-resistance measurement hexagonal plates Ni-NiO sample showed a anomaly in the data at 250 K which vanished at higher magnetic field. Possible reason for anomaly could be the magnetic interactions at grain boundaries [16] which vanished at high magnetic field.

Liquid exfoliation of SrRu_2O_6 and Na_2IrO_3 gave 1-2 μm size 2D sheets in case of SrRu_2O_6 and 200nm size rectangular 2D sheets in case of Na_2IrO_3 . Therefore, it seems that liquid exfoliation of bulk sample into 2D sheets for SrRu_2O_6 and Na_2IrO_3 is possible. Exfoliation process has been checked for reproducibility as well as yield factor for multiple times in both the compounds. Further experiments are required to verify 2D character and possible deviations of properties from bulk sample.

6.2 Future Plans

1. Raman measurements on 2D sheets to see possible shift of peaks in Raman spectra.
2. AFM and/or STM to see thickness of single or multiple sheets.
3. Clean M-H and heat capacity measurements on SrRu_2O_6 to see possible spin flop transition through M-H and verify Néel temperature through heat capacity measurements.
4. Synthesis of unambiguous micron size rodlike Ni-NiO crystals for verification of FIT mechanism in this system and slope change at 250K in resistivity data.

References

- [1] É. Du Trémolet de Lacheisserie, D. Gignoux, M. Schlenker, Magnetism, Magnetism, Edited by E. du Trémolet de Lacheisserie, D. Gignoux, and M. Schlenker. ISBN 0-387-23062-9. Berlin: Springer, 2006.
- [2] M. Fowler, Historical beginnings of theories of electricity and magnetism, *Recuperado el 23 (5) (1997) 2012*.
- [3] N. W. Ashcroft, N. D. Mermin, S. Rodriguez, *Solid state physics (1978)*.
- [4] C. Kittel, *Introduction to solid state physics*, John Wiley and Sons, Inc., UK.
- [5] M-h.
URL <http://hyperphysics.phy-astr.gsu.edu/hbase/Solids/hyst.html>
- [6] M-t.
URL <https://en.wikipedia.org/wiki/Magnetochemistry>
- [7] W. Witczak-Krempa, G. Chen, Y. B. Kim, L. Balents, Correlated quantum phenomena in the strong spin-orbit regime, *Annu. Rev. Condens. Matter Phys.* 5 (1) (2014) 57–82.
- [8] D. J. Singh, Electronic structure and the origin of the high ordering temperature in SrRu_2O_6 , *Physical Review B* 91 (21) (2015) 214420.
- [9] M. J. Gingras, *Introduction to frustrated magnetism (2011)*.
- [10] S.-W. Chen, S.-W. Fu, C.-W. Pao, J.-M. Lee, S.-A. Chen, S.-C. Haw, J.-F. Lee, C.-H. Liu, C.-K. Chang, Y.-C. Chuang, et al., Low temperature structural anomalies arising from competing exchange interactions in pyrochlore $\text{Nd}_2\text{Ru}_2\text{O}_7$ probed by xrd and exafs, *Physical Chemistry Chemical Physics* 17 (36) (2015) 23667–23673.

- [11] J.-G. J. Zhu, C. Park, Magnetic tunnel junctions, *Materials Today* 9 (11) (2006) 36–45.
- [12] E. W. Lee, Magnetostriction and magnetomechanical effects, *Reports on progress in physics* 18 (1) (1955) 184.
- [13] R. D. James, M. Wuttig, Magnetostriction of martensite, *Philosophical Magazine A* 77 (5) (1998) 1273–1299.
- [14] J. Juvonen, A. Nishina, S. Graham, Peer harassment, psychological adjustment, and school functioning in early adolescence, *Journal of educational psychology* 92 (2) (2000) 349–359.
- [15] G. Strijkers, Y. Ji, F. Yang, C. Chien, J. Byers, Andreev reflections at metal/superconductor point contacts: Measurement and analysis, *Physical Review B* 63 (10) (2001) 104510.
- [16] A. Bajpai, A. K. Nigam, Fluctuation-induced tunneling conductance and enhanced magnetoresistance in polycrystalline cro_2 and its composites, *Phys. Rev. B* 75 (2007) 064403. doi:10.1103/PhysRevB.75.064403.
URL <http://link.aps.org/doi/10.1103/PhysRevB.75.064403>
- [17] P. Das, A. Bajpai, Y. Ohno, H. Ohno, J. Müller, On the influence of nanometer-thin antiferromagnetic surface layer on ferromagnetic cro_2 , *Journal of Applied Physics* 112 (5) (2012) 053921.
- [18] V. Nicolosi, M. Chhowalla, M. G. Kanatzidis, M. S. Strano, J. N. Coleman, Liquid exfoliation of layered materials, *Science* 340 (6139) (2013) 1226419.
- [19] Z. Lin, A. McCreary, N. Briggs, S. Subramanian, K. Zhang, Y. Sun, X. Li, N. J. Borys, H. Yuan, S. K. Fullerton-Shirey, et al., 2d materials advances: from large scale synthesis and controlled heterostructures to improved characterization techniques, defects and applications, *2D Materials* 3 (4) (2016) 042001.
- [20] O. Lopez-Sanchez, D. Lembke, M. Kayci, A. Radenovic, A. Kis, Ultrasensitive photodetectors based on monolayer mos_2 , *Nature nanotechnology* 8 (7) (2013) 497–501.

- [21] B. Radisavljevic, A. Radenovic, J. Brivio, i. V. Giacometti, A. Kis, Single-layer mos₂ transistors, *Nature nanotechnology* 6 (3) (2011) 147–150.
- [22] Q. H. Wang, K. Kalantar-Zadeh, A. Kis, J. N. Coleman, M. S. Strano, Electronics and optoelectronics of two-dimensional transition metal dichalcogenides, *Nature nanotechnology* 7 (11) (2012) 699–712.
- [23] W. Sik Hwang, M. Remskar, R. Yan, V. Protasenko, K. Tahy, S. Doo Chae, P. Zhao, A. Konar, H. Xing, A. Seabaugh, et al., Transistors with chemically synthesized layered semiconductor ws₂ exhibiting 105 room temperature modulation and ambipolar behavior, *Applied Physics Letters* 101 (1) (2012) 013107.
- [24] J. Wang, G. Li, L. Li, Synthesis strategies about 2d materials, *TWO-DIMENSIONAL MATERIALS* (2016) 1.
- [25] M. Yi, Z. Shen, A review on mechanical exfoliation for the scalable production of graphene, *Journal of Materials Chemistry A* 3 (22) (2015) 11700–11715.
- [26] M. Osada, T. Sasaki, Two-dimensional dielectric nanosheets: Novel nanoelectronics from nanocrystal building blocks, *Advanced Materials* 24 (2) (2012) 210–228.
- [27] C. I. Hiley, D. Scanlon, A. Sokol, S. Woodley, A. Ganose, S. Sangiao, J. De Teresa, P. Manuel, D. Khalyavin, M. Walker, et al., Antiferromagnetism at $t > 500$ k in the layered hexagonal ruthenate srru₂o₆, *Physical Review B* 92 (10) (2015) 104413.
- [28] W. Tian, C. Svoboda, M. Ochi, M. Matsuda, H. Cao, J.-G. Cheng, B. Sales, D. Mandrus, R. Arita, N. Trivedi, et al., High antiferromagnetic transition temperature of the honeycomb compound srru₂o₆, *Physical Review B* 92 (10) (2015) 100404.
- [29] C. I. Hiley, M. R. Lees, J. M. Fisher, D. Thompsett, S. Agrestini, R. I. Smith, R. I. Walton, Ruthenium (v) oxides from low-temperature hydrothermal synthesis, *Angewandte Chemie International Edition* 53 (17) (2014) 4423–4427.
- [30] Y. Singh, P. Gegenwart, Antiferromagnetic mott insulating state in single crystals of the honeycomb lattice material na₂iro₃, *Physical Review B* 82 (6) (2010) 064412.
- [31] A. Kitaev, Anyons in an exactly solved model and beyond, *Annals of Physics* 321 (1) (2006) 2–111.

- [32] S. N. Gupta, P. Sriluckshmy, K. Mehlawat, A. Balodhi, D. K. Mishra, D. Muthu, S. Hassan, Y. Singh, T. Ramakrishnan, A. Sood, Raman signatures of strong kitaev exchange correlations in $(\text{Na}_{1-x}\text{Li}_x)_2\text{IrO}_3$: Experiments and theory, arXiv preprint arXiv:1408.2239.
- [33] S. Choi, R. Coldea, A. Kolmogorov, T. Lancaster, I. Mazin, S. Blundell, P. Radaelli, Y. Singh, P. Gegenwart, K. Choi, et al., Spin waves and revised crystal structure of honeycomb iridate Na_2IrO_3 , Physical review letters 108 (12) (2012) 127204.
- [34] Powder xrd.
URL http://images.slideplayer.com/15/4616826/slides/slide_10.jpg
- [35] Sem.
URL https://en.wikipedia.org/wiki/Scanning_electron_microscope
- [36] Raman spectroscopy.
URL https://en.wikipedia.org/wiki/Raman_spectroscopy
- [37] Squid.
URL http://squid.iitd.ernet.in/Basic_Literature.htm
- [38] Ppms.
URL https://www.mrl.ucsb.edu/sites/default/files/mrl_docs/instruments/resPPMS.pdf
- [39] Z. Pchelkina, S. Streltsov, I. Mazin, Spectroscopic signatures of molecular orbitals on a honeycomb lattice, arXiv preprint arXiv:1607.08847.
- [40] L. Kock, D. De Waal, Raman analysis of ancient pigments on a tile from the citadel of algiers, Spectrochimica Acta Part A: Molecular and Biomolecular Spectroscopy 71 (4) (2008) 1348–1354.
- [41] K. Biswas, C. Rao, Synthesis and characterization of nanocrystals of the oxide metals, RuO_2 , IrO_2 , and ReO_3 , Journal of nanoscience and nanotechnology 7 (6) (2007) 1969–1974.
- [42] P. A. Temple, C. Hathaway, Multiphonon raman spectrum of silicon, Physical Review B 7 (8) (1973) 3685.

- [43] J. W. Krizan, J. H. Roudebush, G. M. Fox, R. J. Cava, The chemical instability of Ni_2Fe_3 in air, *Materials Research Bulletin* 52 (2014) 162–166.
- [44] X. Ni, Q. Zhao, D. Zhang, X. Zhang, H. Zheng, Novel hierarchical nanostructures of nickel: self-assembly of hexagonal nanoplatelets, *The Journal of Physical Chemistry C* 111 (2) (2007) 601–605.
- [45] L. Hu, R. Zhang, Q. Chen, Synthesis and assembly of nanomaterials under magnetic fields, *Nanoscale* 6 (23) (2014) 14064–14105.
- [46] Q. Wang, B. Geng, S. Wang, J. Liu, Z. Cheng, D. Si, A facile sonochemical route to morphology controlled nickel complex mesostructures, *CrystEngComm* 11 (7) (2009) 1317–1322.
- [47] Nioraman.
URL <http://rruff.info/bunsenite/display=default/>
- [48] N. Mironova-Ulmane, A. Kuzmin, I. Steins, J. Grabis, I. Sildos, M. Pärns, Raman scattering in nanosized nickel oxide NiO , in: *Journal of Physics: Conference Series*, Vol. 93, IOP Publishing, 2007, p. 012039.
- [49] L. Courtade, C. Turquat, C. Muller, J. Lisoni, L. Goux, D. Wouters, D. Goguenheim, P. Roussel, L. Ortega, Oxidation kinetics of Ni metallic films: formation of NiO -based resistive switching structures, *Thin solid films* 516 (12) (2008) 4083–4092.